**NTNU – Trondheim**
Norwegian University of
Science and Technology

# Large Area Patterning of Embedded Magnetic Nanostructures in Complex Oxide Thin Films

**Aksel Skauge Mellbye**

Nanotechnology
Submission date: June 2015
Supervisor: Jostein Grepstad, IET
Co-supervisor: Erik Folven, IET
Ambjørn Dahle Bang, IET

Norwegian University of Science and Technology
Department of Electronics and Telecommunications

# Abstract

Complex oxide materials exhibit a wide range of functional properties, making them interesting for future use in electronic and spintronic devices. Through nanopatterning of thin film structures, magnetic shape effects can be investigated.

A novel patterning method, combining substrate conformal imprint lithography (SCIL) with ion implantation, was used to pattern areas up to $7.5 \times 7.5\,mm^2$ of identical ferromagnetic nanoscale lines in thin films of $La_{0.7}Sr_{0.3}MnO_3$ (LSMO) and $LaFeO_3$ (LFO). The pattern had a linewidth of 160 nm and a pitch of 400 nm, and the lines were embedded in a paramagnetic matrix. In order to perform SCIL on square substrates, an adapter was manufactured in order for the samples to fit on a two-inch SCIL wafer chuck.

A dual-layer mask of Amonil and PMMA resists with a total thickness of approximately 180 nm was shown to work successfully as an implantation mask for 50 keV $Ar^+$ ions that disrupted the magnetic order of the unprotected areas of the thin film.

Investigation of the patterned thin film by atomic force microscopy (AFM) and vibrating sample magnetometry (VSM) shows that the patterning process yields high-quality ferromagnetic nanostructures with clear shape-induced magnetic anisotropy. The nanoscale pattern in the thin film shows a saturation magnetic moment of $3.2\,\mu_B/Mn$, which is somewhat lower than the bulk value of $3.7\,\mu_B/Mn$. Parallel to the nanoscale line pattern, a coercivity of 290 Oe was measured at 50 K, while a coercivity of 125 Oe was measured perpendicular to the line pattern.

# Sammendrag

Komplekse oksider er materialer med mange funksjonelle egenskaper, hvilket gjør dem interessante for framtidig bruk i elektroniske og spintroniske komponenter. Ved å produsere nanoskala mønster i tynnfilmer, kan effekten materialets form har på dets magnetiske egenskaper undersøkes.

Identiske ferromagnetiske nanoskala strukturer som dekker områder opp til $7.5 \times 7.5\,\mathrm{mm}^2$ ble produsert ved hjelp av en ny metode, der substratkonform imprintlitografi (SCIL) ble kombinert med ioneimplantering. Et ferromagnetisk nanoskala linjemønster med linjebredde 160 nm og periode 400 nm adskilt av paramagnetiske områder ble produsert i tynnfilmer av $La_{0.7}Sr_{0.3}MnO_3$ (LSMO) og $LaFeO_3$ (LFO). For å gjøre SCIL på kvadratiske substrater, måtte et adapter fabrikeres for å kunne plassere prøvene på en SCIL-prøveholder tilpasset to-tommers skiver.

En tolags maske av Amonil- og PMMA-resister med en total tykkelse på omtrent 180 nm ble med suksess brukt som implanteringsmaske for 50 keV $Ar^+$-ioner som fjernet den magnetiske orden i de ubeskyttede områdene av tynnfilmen.

Målinger av den mønstrede tynnfilmen med atomkraftmikroskopi (AFM) og vibrerende magnometri (VSM) viser at mønstringsprosessen gir ferromagnetiske nanostrukturer av høy kvalitet med klar magnetisk anisotropi på grunn av mønsteret. Det nanoskala mønsteret i tynnfilmen har metningsmagnetisering på $3.2\,\mu_B/\mathrm{Mn}$, som er noe lavere enn metningsmagnetiseringen i bulk på $3.7\,\mu_B/\mathrm{Mn}$. En koersivitet på 290 Oe ble målt ved 50 K parallelt med linjemønsteret, mens en koersivitet på 125 Oe ble målt normalt på linjene.

# Preface

This thesis is submitted in partial fulfillment of the requirements for the degree of Master of Science in Nanotechnology from the Norwegian University of Science and Technology. The work presented herein has been performed during the spring of 2015 with the Oxide Electronics group of the Department of Electronics and Telecommunications. Experimental work was performed in the NTNU NanoLab cleanroom facilities, as well as in department laboratories.

The Research Council of Norway is acknowledged for the support to NTNU NanoLab through the Norwegian Micro- and Nano-Fabrication Facility, NorFab (197411/V30).

An appendix with instructions for performing SCIL on the SUSS MA6 at NTNU NanoLab was written during this project, in order to ensure that knowledge of the quirks of operating the MA6 in SCIL mode are preserved for future users of the instrument. During my project and Master's thesis work, I have gotten to know the instrument and many of its undocumented software bugs. I have also explored the parameter space of the instrument, allowing me to give recommendations to new users for some of the software parameters. As I am leaving, there are no experienced SCIL users left at NTNU NanoLab. This written guide will therefore hopefully be useful for future SCIL users, allowing them to get quickly up to speed, and not spend as much time as me struggling with the instrument.

I would like to extend my deepest thanks to my supervisors *Jostein Kvaal Grepstad* and *Erik Folven* for their advice and support troughout the project, and to *Ambjørn Dahle Bang* for invaluable assistance in the cleanroom.

I would also like to thank *Peter Køllensperger* for kindly lending me the nanoimprint master wafer used in this work, and *Fredrik Kjemperud Olsen* for growing thin film samples and helping me with vibrating sample magnetometer measurements. I would also like to thank the staff at NTNU NanoLab, for being helpful and supportive throughout the project.

Finally, I would like to thank *Simen Martinussen*, *Vetle Meland Risinggård* and the other students at MTNANO for inspiring conversations, fruitful discussions and for making the past five years a blast.

June 11, 2015
NTNU, Trondheim

Aksel Skauge Mellbye

# Contents

**Abstract** iii

**Sammendrag** v

**Preface** vii

**Contents** ix

**Glossary** xi

**List of Figures** xiii

**List of Tables** xv

**1 Introduction** 1
- 1.1 Motivation 1
- 1.2 Background 1
- 1.3 Project Outline 2

**2 Micromagnetics** 5
- 2.1 Theory of Magnetism 5
  - 2.1.1 Magnetic Materials 5
  - 2.1.2 Exchange Interactions 8
  - 2.1.3 Magnetic Domains 9
  - 2.1.4 Magnetic Hysteresis 10
  - 2.1.5 Magnetic Anisotropy 11
- 2.2 Perovskite Oxides 13
  - 2.2.1 Lanthanum Strontium Manganite 14
  - 2.2.2 Lanthanum Ferrite 15
  - 2.2.3 LFO/LSMO Bilayers 15

**3 Experimental Methods** 17
- 3.1 Sample Preparation 17
  - 3.1.1 Overview 17
  - 3.1.2 Substrate Conformal Imprint Lithography 18

3.1.3 Reactive Ion Etching . . . . . 25
3.1.4 Ion Implantation . . . . . 26
3.1.5 Process Recipe . . . . . 27
3.2 Characterization . . . . . 30
3.2.1 Overview . . . . . 30
3.2.2 Scanning Probe Microscopy . . . . . 30
3.2.3 Vibrating Sample Magnetometer . . . . . 31

**4 Results and Discussion 35**
4.1 SCIL Stamp Replication . . . . . 35
4.2 SCIL Adapter Development . . . . . 36
4.2.1 Blind Hole Adapters . . . . . 36
4.2.2 Through Hole Adapters . . . . . 37
4.3 SCIL Process Development . . . . . 38
4.3.1 Residual Layer Thickness . . . . . 38
4.3.2 Residual Layer Etch . . . . . 39
4.4 Thin Film Patterning . . . . . 41
4.4.1 Thin Film Growth . . . . . 41
4.4.2 Substrate Conformal Imprint Lithography . . . . . 41
4.4.3 Ion Implantation and Mask Removal . . . . . 42
4.4.4 Characterization . . . . . 44
4.5 Magnetic Characterization of Thin Film Samples . . . . . 44
4.5.1 Diamagnetic Contribution . . . . . 44
4.5.2 Saturation Magnetic Moment . . . . . 46
4.5.3 Magnetic Hysteresis . . . . . 50
4.6 Further Process Development . . . . . 54

**5 Conclusion and Outlook 57**
5.1 Outlook . . . . . 57

**Bibliography 59**

**Appendices 63**

**A SCIL on the SUSS MA6 65**
A.1 SCIL Wafer Chuck Alignment . . . . . 65
A.2 General Considerations . . . . . 65
A.3 MA6 Conversion to SCIL Mode . . . . . 66
A.4 Performing SCIL . . . . . 68
A.4.1 Notes on SCIL Process Parameters . . . . . 70
A.4.2 Aborting an Imprint . . . . . 71
A.5 MA6 Conversion to Lithography Mode . . . . . 72
A.6 Troubleshooting . . . . . 72

**B Raw VSM Data 73**

# Glossary

**AFM** atomic force microscope.

**bcc** body-centered cubic.

**DUV** deep UV.

**EBL** electron beam lithography.

**fcc** face-centered cubic.

**ICP-RIE** inductively-coupled plasma reactive ion etching.

**LFO** lanthanum ferrite.

**LSMO** lanthanum strontium manganite.

**MRT** master replication tool.

**NIL** nanoimprint lithography.

**PDMS** poly(dimethylsiloxane).

**PEEM** photoemission electron microscopy.

**PLD** pulsed laser deposition.

**PMMA** poly(methyl methacrylate).

**POT** peel-off tool.

**RHEED** reflection high-energy electron diffraction.

**RIE** reactive ion etching.

**SCIL** substrate conformal imprint lithography.

**SE** secondary electron.

**SEM** scanning electron microscope.

**SRIM** Stopping and Range of Ions in Matter.

**STM** scanning tunneling microscope.

**STO** strontium titanate.

**T-NIL** thermoplastic nanoimprint lithography.

**UV-NIL** UV-cured nanoimprint lithography.

**VSM** vibrating sample magnetometer.

**WEC** wedge error compensation.

**XMCD** x-ray magnetic circular dichroism.

**XMLD** x-ray magnetic linear dichroism.

# List of Figures


2.1 Magnetic ordering behavior . . . . . . . . . . . . . . . . . . . . . . . . . . . . 6
2.2 Types of antiferromagnets . . . . . . . . . . . . . . . . . . . . . . . . . . . . 7
2.3 Superexchange mechanism in manganese oxide . . . . . . . . . . . . . . . . . 8
2.4 Double exchange mechanism in a manganite . . . . . . . . . . . . . . . . . . 9
2.5 Domain walls . . . . . . . . . . . . . . . . . . . . . . . . . . . . . . . . . . . 10
2.6 Magnetic hysteresis . . . . . . . . . . . . . . . . . . . . . . . . . . . . . . . 11
2.7 Illustration of shape anisotropy . . . . . . . . . . . . . . . . . . . . . . . . . 12
2.8 Effect of exchange coupling on hysteresis . . . . . . . . . . . . . . . . . . . . 13
2.9 Ideal perovskite unit cell . . . . . . . . . . . . . . . . . . . . . . . . . . . . 14

3.1 Process flow . . . . . . . . . . . . . . . . . . . . . . . . . . . . . . . . . . . 18
3.2 Illustration of a SCIL stamp . . . . . . . . . . . . . . . . . . . . . . . . . . 19
3.3 SCIL imprint and separation sequences. . . . . . . . . . . . . . . . . . . . . 20
3.4 4-inch (100 mm) Eulitha silicon master wafer . . . . . . . . . . . . . . . . . 21
3.5 Complete SCIL stamp with rubber frame and glass backing . . . . . . . . . 22
3.6 Illustration of polycarbonate adapter in wafer chuck . . . . . . . . . . . . . 23
3.7 Polycarbonate adapter designs . . . . . . . . . . . . . . . . . . . . . . . . . 24
3.8 SCIL adapter with sample and blue tape on backside . . . . . . . . . . . . . 24
3.9 Illustration of through hole adapter on wafer chuck . . . . . . . . . . . . . . 25
3.10 Schematic of an ICP-RIE tool . . . . . . . . . . . . . . . . . . . . . . . . . 27
3.11 Illustration of an AFM. . . . . . . . . . . . . . . . . . . . . . . . . . . . . 31
3.12 Schematic of a vibrating sample magnetometer . . . . . . . . . . . . . . . . 32
3.13 Sample P50319 with outline for area measurement drawn in ImageJ . . . 33
3.14 Magnetic field **H** applied to the sample in different orientations . . . . . . 34

4.1 SEM image of SCIL stamp . . . . . . . . . . . . . . . . . . . . . . . . . . . 36
4.2 Partial imprints . . . . . . . . . . . . . . . . . . . . . . . . . . . . . . . . . 37
4.3 SEM images of residual layer thickness . . . . . . . . . . . . . . . . . . . . . 38
4.4 SEM image of residual layer thickness . . . . . . . . . . . . . . . . . . . . . 40
4.5 SEM image of residual layer after etch . . . . . . . . . . . . . . . . . . . . . 40
4.6 SEM images of residual layer after etch . . . . . . . . . . . . . . . . . . . . 41
4.7 AFM image of sample after thin film growth . . . . . . . . . . . . . . . . . 42
4.8 Sample P50139 at different stages of processing . . . . . . . . . . . . . . . . 43
4.9 $1.6 \times 1.6\,\mu m^2$ AFM image of line pattern . . . . . . . . . . . . . . . . . . . 45

4.10 $15 \times 15\,\mu m^2$ AFM image of line pattern . . . . . 46
4.11 Hysteresis curves showing diamagnetism at high applied field . . . . . 47
4.12 Saturation magnetic moment vs. temperature . . . . . 48
4.13 Hysteresis curve above $T_c$ . . . . . 50
4.14 Hysteresis curves for unpatterned control sample . . . . . 51
4.15 Hysteresis curves parallel to pattern . . . . . 52
4.16 Hysteresis curves perpendicular to pattern . . . . . 53
4.17 Coercive field . . . . . 54
4.18 Remanent magnetization . . . . . 55

A.1 SUSS SCIL subassembly . . . . . 66
A.2 Close-up of o-rings . . . . . 67
A.3 SCIL load frame mounted on mask aligner. . . . . . 67
A.4 SCIL stamp fixed to SCIL mask holder. . . . . . 68
A.5 SCIL connector block . . . . . 69
A.6 UV optometer . . . . . 69
A.7 SCIL wafer chuck with adapter loaded into MA6. . . . . . 70
A.8 SUSS MA6 mask aligner with SCIL subunit during exposure. . . . . . 70

B.1 Hysteresis curve of unpatterned control sample . . . . . 73
B.2 Hysteresis curves parallel with pattern . . . . . 74
B.3 Hysteresis curves perpendicular to pattern . . . . . 75
B.4 Saturation magnetic moment as a function of temperature . . . . . 76
B.5 Hysteresis curve above $T_c$ . . . . . 77

# List of Tables

3.1 Process parameters for SCIL imprinting . . . . . . . . . . . . . . . . . . . . 29
3.2 Process parameters for ICP-RIE etch . . . . . . . . . . . . . . . . . . . . . . 30

A.1 List of process parameters in MA6 software with description. . . . . . . . . 71

# Chapter 1

# Introduction

## 1.1 Motivation

The invention of the transistor in 1947 marked the beginning of an era of solid-state electronics [1]. With the discovery of the giant magnetoresistive effect (GMR) in 1988, a new field of spin-based electronics (spintronics) was born [2]. In spintronic devices, the information carrier is the electron spin, rather than the electron charge. This creates opportunities for a new generation of devices, where the interaction between the magnetic properties of the material and the spin of the carrier electron give rise to spin-dependent effects.

Giant magnetoresistance, as well as tunnel magnetoresistance (TMR), are examples of such spin-dependent effects, and are the basis of the read heads in modern hard disk drives. TMR, which appears in magnetic tunnel junctions and spin valves, is also the basis of several other applications of spintronics, such as magnetic random access memory (MRAM) [3]. Such devices rely on multilayers of magnetic thin films, where an uncompensated antiferromagnetic layer serves to pin the magnetization of an adjacent ferromagnetic layer by an effect known as *exchange bias*.

Since the 1990s, interest has grown for transition metal oxides that exhibit colossal magnetoresistance (CMR), that is, a large change in electrical resistance in the presence of a magnetic field. The majority of studies have focused on the manganese perovskites $T_{1\text{-}x}D_xMnO_3$ where T is a trivalent lanthanide cation and D is a divalent cation [4]. Utilizing the magnetoresistive and hysteretic behavior of these materials, it could be possible to create new spintronic devices with novel properties and uses.

## 1.2 Background

Recently, the properties of epitaxial thin films of lanthanum strontium manganite (LSMO) and lanthanum ferrite (LFO), as well as the interactions between bilayers of the two materials, have been investigated. While LSMO is ferromagnetic at typical doping concentrations of strontium, LFO is antiferromagnetic. Through the patterning of micro- and nanoscale magnetic structures in the thin films, the effect of geometry, size and orientation of the magnetic nanostructures relative to the crystalline axes has

been investigated [5–10].

Takamura *et al.* [5] have demonstrated a method for nanostructuring thin films of LSMO and LFO grown on a substrate of strontium titanate (STO) by pulsed laser deposition (PLD). Using electron beam lithography (EBL), nanoscale structures were defined in HSQ [5] or poly(methyl methacrylate) (PMMA) [6] resists. Since HSQ is a negative resist, the pattern could be used directly as a mask for ion implantation. When using a PMMA resist, a lift-off process with chromium was used in order to invert the pattern before ion implantation. The ion implantation step utilized 50 keV $Ar^+$ ions to disrupt the magnetic order of the uncovered parts of the thin film, leaving isolated nanoscale magnetic structures in a paramagnetic matrix.

The magnetic properties of such nanoscale magnetic structures have been investigated. Using a combination of polarized x-ray absorption spectroscopy and photoemission electron microscopy (PEEM), images of the microscopic domain structure of the nanoscale magnets have been acquired. Relying on x-ray magnetic linear dichroism (XMLD), it is possible to achieve contrast between antiferromagnetic domains of different orientation [6, 7, 9], while x-ray magnetic circular dichroism (XMCD) gives contrast between ferromagnetic domains of different orientation [5].

However, in order to perform macroscopic measurements of the magnetic properties of such structures, such as measurement of magnetic hysteresis curves using a vibrating sample magnetometer (VSM), large areas of identical structures are necessary in order to achieve a sufficient magnetic signal. The signal from the nanoscale pattern also needs to be representative of the sample as a whole. EBL, which is a maskless, direct-write method, has the disadvantage of long writing times when a large area is to be patterned. In addition, EBL exposures consist of several *write fields* that need to be stitched together during exposure. This necessarily leads to *stitching errors* along the edges of the write field, where there is a discontinuity in the pattern. For certain patterns, such as long lines that are larger than a single write field, this leads to imperfect pattern replication.

## 1.3 Project Outline

In this thesis, a novel method for patterning large areas of ferromagnetic and antiferromagnetic nanostructures embedded in a paramagnetic matrix is presented. Substrate conformal imprint lithography (SCIL), a new (2009) technique for nanoimprint lithography (NIL), has been employed to create a nanoscale line pattern covering the entire surface of $7.5 \times 7.5\,\mathrm{mm}^2$ samples consisting of LSMO and LFO thin films epitaxially grown on STO substrates. This patterning step has been used instead of the EBL patterning step in the process developed by Takamura *et al.* [5] in order to be able to pattern the entire area of the sample. The development process for an adapter that was needed in order to perform SCIL on square samples is also reported. Magnetic measurements have then been performed on the patterned samples using a VSM.

This thesis consists of five chapters. After this introduction, Chapter 2 gives a short introduction to magnetic phenomena in solid materials, with focus on the magnetic properties of LSMO and LFO. Chapter 3 gives an overview of the instruments used for the patterning process, as well as a complete process recipe. Then, an overview of

the characterization tools as well as the methodology for magnetic characterization by VSM is given. Chapter 4 covers the results of the development of a working process for SCIL on square substrates, as well as results of the patterning process and subsequent magnetic characterization of thin film samples. The conclusions are summarized in Chapter 5.

# Chapter 2

# Micromagnetics

*This chapter contains the theory required to explain the occurence of magnetic behavior in nanoscale magnetic structures of perovskite oxides. First, an introduction to magnetism, and in particular ferromagnetism and antiferromagnetism will be given. Then, an introduction to perovskite oxides and the magnetic phenomena in* $La_{1\text{-}x}Sr_xMnO_3$ *and* $LaFeO_3$ *is given. Parts of this text has been adapted from Mellbye [11], as this is a continuation of that work.*

## 2.1 Theory of Magnetism[1]

Magnetism is a physical phenomenon that is mediated by magnetic fields. From electromagnetism, we have that a moving electric charge induces a magnetic field. On the microscopic level, magnetic moments and fields are induced by the movement of electrons around the atomic nucleus. In addition to the orbital motion of electrons around the nucleus, electrons have an intrinsic property known as the *spin*. The combined effect gives the electron magnetic moment

$$\mu = -g\mu_B \mathbf{J} \tag{2.1}$$

where g is the *gyromagnetic ratio*, $\mathbf{J}$ is the total electron angular momentum, and $\mu_B = \frac{e\hbar}{2m_e c} = 9.724 \cdot 10^{-21}$ erg/G is the *Bohr magneton*.

### 2.1.1 Magnetic Materials

In materials, the atomic orbitals fill according to *Hund's rules*, which say that the lowest energy state is the one with the maximum multiplicity. This means that each orbital is filled with one unpaired electron, before a second electron with opposite spin is added to each orbital, in accordance with the Pauli exclusion principle. From this, we have that a material needs to have partially filled orbitals in order to have a net magnetic moment. Most magnetic materials are therefore compounds of transition metals or lanthanides, with partially filled *d* and *f* orbitals, respectively. The different

[1] This section is based on O'Handley [12] and Kittel [13], unless otherwise indicated.

ordering phenomena that occur on the microscopic scale are complex, but their results are easily observed through the macroscopic magnetic response of the material. Figure 2.1 shows different magnetic ordering behaviors.

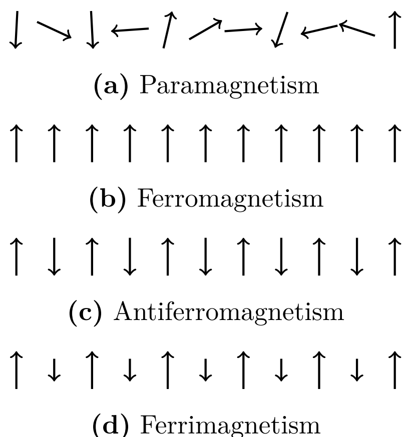

**(a)** Paramagnetism

**(b)** Ferromagnetism

**(c)** Antiferromagnetism

**(d)** Ferrimagnetism

**Figure 2.1:** Magnetic ordering behavior

#### Diamagnetism

All materials exhibit a tendency to oppose an applied magnetic field. This is known as diamagnetism. Semiclassically, it can be described by considering a magnetic field $\mathbf{B}$ applied to an electron. This gives rise to *Larmor precession*, due to a torque $\Gamma = \mu \times \mathbf{B}$ being exerted on the electron. This precession of the electron leads to an induced field in the opposite direction of the applied field. Diamagnetic materials have a magnetic susceptibility $\chi_m < 0$. The diamagnetic response is weak compared to other magnetic responses. Only materials that do not exhibit stronger magnetic phenomena are therefore classified as diamagnetic.

#### Paramagnetism

Atoms with partially filled orbitals have a permanent magnetic moment, due to the spin of unpaired electrons. In an applied magnetic field, the magnetic moments have a tendency to align with the applied field. However, in the absence of an applied field, random thermal motion will randomize the spin orientations. Paramagnetic materials have a magnetic susceptibility $\chi_m > 0$.

#### Ferromagnetism

Some materials, in addition to being paramagnetic, also exhibit a tendency for the magnetic moments to align parallel to each other, even in the absence of an applied

magnetic field. This is known as *ferromagnetism*. Above the Curie temperature, $T_C$, ferromagnetic order vanishes, and the material becomes paramagnetic. Common ferromagnets include iron, nickel, cobalt, and some alloys of rare earth metals. The cause of the spontaneous alignment of magnetic moments in a ferromagnetic material is known as the *exchange interaction*, and will be described in further detail in Section 2.1.2.

### Antiferromagnetism

Like ferromagnetism, *antiferromagnetism* is a manifestation of magnetic order. In antiferromagnetic materials, the magnetic moments align in a regular pattern where neighboring spins point in opposite directions. Above the Néel temperature, $T_N$, the antiferromagnetic order vanishes, and the material becomes paramagnetic. When no external field is applied, the total magnetization of an antiferromagnet is zero. Exchange interactions between spins at neighboring lattice sites are, like in the case of ferromagnetism, the cause of antiferromagnetism. It is, however, impossible for a crystal to have antiferromagnetic order in all directions. Along certain crystallographic directions, parallel ordering will occur. Depending on which crystallographic planes are ferromagnetically ordered, the material can be classified as an A-, C- or G-type antiferromagnet. Figure 2.2 illustrates the different classes of antiferromagnets.

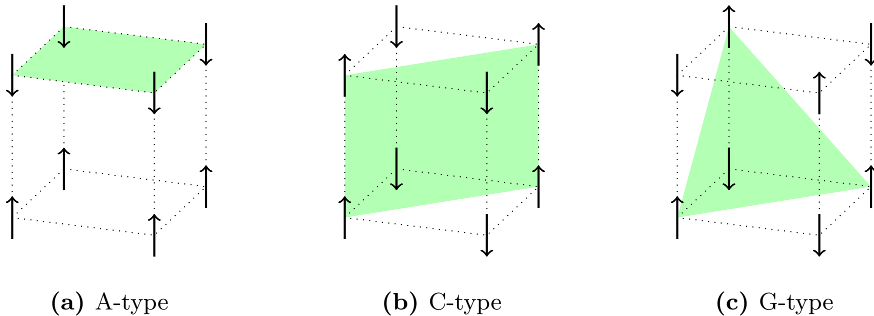

**(a)** A-type **(b)** C-type **(c)** G-type

**Figure 2.2:** Types of antiferromagnets. Ferromagnetic planes are highlighted in green. A-type: Ferromagnetic ordering along (100) planes. C-type: Ferromagnetic ordering along (110) planes. G-type: Ferromagnetic ordering along (111) planes.

### Ferrimagnetism

A ferrimagnetic material is a material with opposing magnetic moments, like in antiferromagnetism, but where the opposing moments are unequal, and a net magnetization remains. A common cause of this is when the material consists of different materials or ions, such as $Fe^{2+}$ and $Fe^{3+}$ in magnetite. Like ferromagnets, ferrimagnets become paramagnetic above the Curie temperature $T_C$.

### 2.1.2 Exchange Interactions

#### Direct Exchange

The direct exchange interaction can be derived by considering a system of several atoms obeying Fermi statistics. The Heisenberg exchange Hamiltonian can be written as

$$\mathcal{H}_{\text{Heis}} = -\sum_{i,j} J\vec{s}_i \cdot \vec{s}_j \tag{2.2}$$

where $\vec{s}_i$ represents the spin of electron $i$, and $J$ is the exchange constant. It follows that a positive value of $J$ leads to the exchange energy favoring electrons with parallel spins, causing ferromagnetism. Likewise, a negative value of $J$ leads to the exchange energy favoring electrons with antiparallel spins, causing antiferromagnetism.

The sign of $J$ is dependent on the overlap of the electron wavefunctions and the Coloumb interaction of the electrons with the nuclei of the material. This means that the sign of $J$ is sensitive to the internuclear distance, explaining why only some materials exhibit ordered magnetism.

The given form of the Heisenberg exchange Hamiltonian is generally accepted as a valid starting point for theories of magnetism in insulators, where electrons are localized. In metals with delocalized electrons, however, the direct exchange interaction is not sufficient to explain the observed magnetic behavior. In such materials, an indirect exchange mechanism known as the RKKY interaction is generally accepted as the main mechanism for exchange. Other indirect exchange mechanisms include superexchange and double exchange.

#### Superexchange

Superexchange is a form of indirect exchange, where there is a coupling between two next-nearest neighbor cations through a non-magnetic anion. The superexchange interaction is usually antiferromagnetic, but can also be ferromagnetic, and is dependent on the bond angle between the cations and the anion. Figure 2.3 illustrates the superexchange mechanism in manganese oxide. The $e_g$ orbitals of the manganese ions are antiferromagnetically coupled to the 2p orbital of oxygen, causing an indirect antiferromagnetic coupling between the two manganese ions.

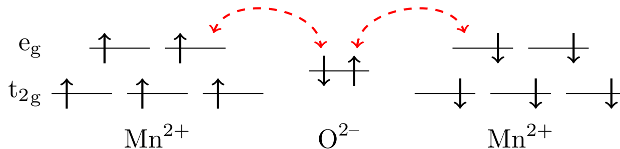


**Figure 2.3:** Superexchange mechanism in manganese oxide. The arrows represent the interaction between the $e_g$ orbitals of manganese and the 2p orbital of oxygen.

### Double Exchange

Double exchange is another form of indirect exchange, which may arise between two ions with differing oxidation states. Double exchange was first proposed by Zener [14, 15] and describes how the electrons on two neighboring cations can couple through an intermediate anion. If the anion gives up one of its electrons to the highly oxidized cation, the vacant orbital can be filled by an electron from the less oxidized cation. The total process can be viewed as the movement of an electron between the neighboring cations with retention of spin. The process is illustrated in Figure 2.4. The ability to delocalize the electrons reduces the energy of the system, leading to a ferromagnetic alignment of neighboring ions.

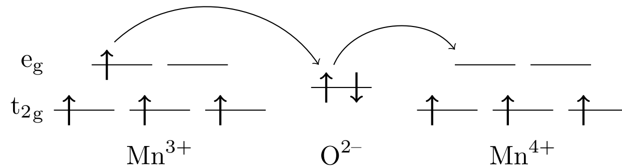


**Figure 2.4:** Double exchange mechanism in a manganite. The arrows illustrate how an electron can move from one species to another while conserving spin. This leads to ferromagnetic alignment of neighboring ions.

## 2.1.3 Magnetic Domains

Although exhibiting ferromagnetic order on the microscopic scale, materials may not have a finite bulk magnetization. This is due to the formation of magnetic domains inside the material. The magnetic moments are parallel within each domain, but the magnetization direction varies between domains. Domain walls form between the different domains, where the magnetic moments gradually change from the magnetization direction of one domain to the direction of the other. Domains form in order to minimize the internal energy of the material. In particular, they form to minimize the *demagnetizing field*, as will be described later. There is however, an energy cost associated with forming a domain wall, as the spins are not aligned with each other across the domain wall. Hence, the formation of domains is energetically favourable only if the energy gain from lowering the magnetostatic energy is greater than the cost of the domain wall.

The thickness of a domain wall depends on the magnetocrystalline anisotropy and exchange energy $J_{ex}$ of the material, but is on average around $100 - 150$ atoms. A Bloch wall is a domain wall where the magnetization rotates through the plane of the domain wall, as illustrated in Figure 2.5a. Bloch walls typicallly appear in bulk materials, where the size of the magnetic material is considerably larger than the width of the domain wall. Néel walls are domain walls where the magnetization rotates in the plane of the domain wall, as illustrated in Figure 2.5b. Néel walls are common in

thin films. If it wasn't for magnetic anisotropy, as will be described in Section 2.1.5, Néel walls would span the whole volume of the material.

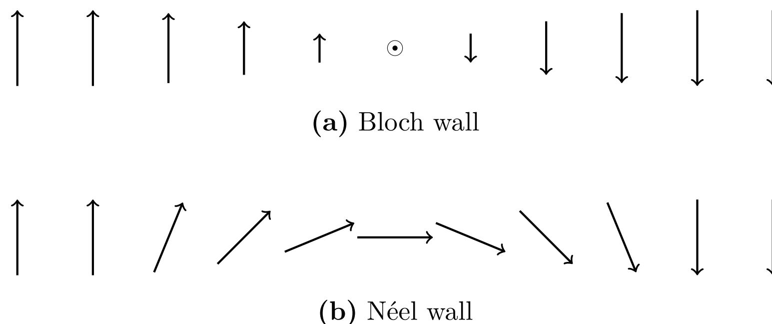

**(a)** Bloch wall

**(b)** Néel wall

**Figure 2.5:** Domain walls. **(a)** Bloch wall, with spins rotating through the plane of the domain wall, i.e. out of the paper plane. **(b)** Néel wall, with spins rotating in the plane of the domain wall, i.e. in the paper plane.

### 2.1.4 Magnetic Hysteresis

As a magnetic field $\mathbf{H}$ is applied to a ferromagnetic material, the domain walls will move, increasing the size of domains with favourable magnetic orientation with respect to the applied field. This movement does not happen continuously, but rather in small, discrete steps known as Barkhausen jumps. In addition, the magnetization direction of the domains will rotate towards the direction of the applied field. As a sufficiently large field is applied, the induced magnetic moment saturates at the saturation magnetization $M_s$. While rotation of domains is a reversible process, domain growth is irreversible. As the applied field is removed, the domain walls may therefore not return to their initial locations. This leads to a remanent magnetization $M_r$ at zero applied field.

In order to reduce the magnetization to zero, a magnetic field $H_c$ in the opposite direction needs to be applied. The magnitude of this field is known as the *coercivity* of the material. The value of the coercivity is the single most sensitive property of ferromagnetic materials which is subject to control, and ranges over seven orders of magnitude, from $2 \cdot 10^{-3}$ Oe for permalloy to $4 \cdot 10^{4}$ Oe for samarium-cobalt [16]. Materials with low coercivity are called *soft* magnetic materials, while those with high coercivity are called *hard* magnetic materials. Figure 2.6 illustrates hysteresis curves for different materials and magnetization directions.

Particles or grains of small sizes, typically below 100 nm, have a significantly higher coercivity than bulk material. This is because the particles are always magnetized to saturation as a single domain, as the flux-closure configuration, as described in Section 2.1.5, is energetically unfavourable. This precludes magnetization reversal via domain wall motion, requiring coherent rotation in order to change the magnetization.

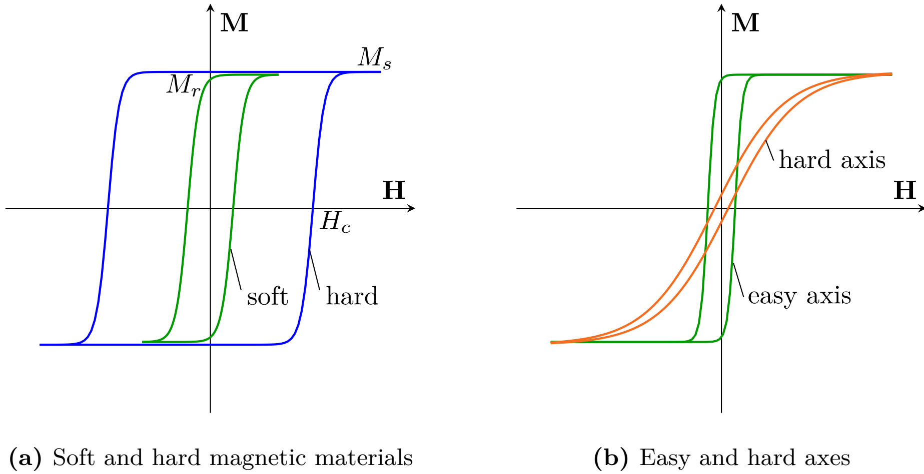


**(a)** Soft and hard magnetic materials

**(b)** Easy and hard axes

**Figure 2.6:** Illustration of magnetic hysteresis in a ferromagnet.

### 2.1.5 Magnetic Anisotropy

It is normally easier to magnetize a material along some directions compared to others. The preference for the magnetization to lie in a particular direction is known as magnetic anisotropy. Magnetic anisotropy can be caused by the shape of the sample, the crystal symmetry, or stresses in the material. A direction along which a material is readily magnetized, is called an *easy axis*, while a direction along which it is difficult to magnetize a material is called a *hard axis*.

#### Shape Anisotropy

Shape anisotropy describes the tendency of magnetization to align along a long axis of a non-spherical object, rather than along a short axis. This is due to the fact that magnetic flux lines escape the sample at the edges of an object, which can be seen as magnetic poles on the surface of the object. The field from these surface poles passing through the sample is called the demagnetizing field and has the tendency to reduce the overall magnetization. The more surface poles, the larger the demagnetizing field, which makes it harder to magnetize the sample along this direction. The demagnetizing field can be written as

$$H_d = -NM \tag{2.3}$$

where $N$ is the demagnetization factor , which is generally a tensor, and $M$ is the magnetization of the object. Figure 2.7 illustrates magnetization along the long and short axes of a rectangular object.

In a thin film material, the thickness of the film is generally much smaller than the dimensions in the plane of the film. Due to shape anisotropy, this means that the

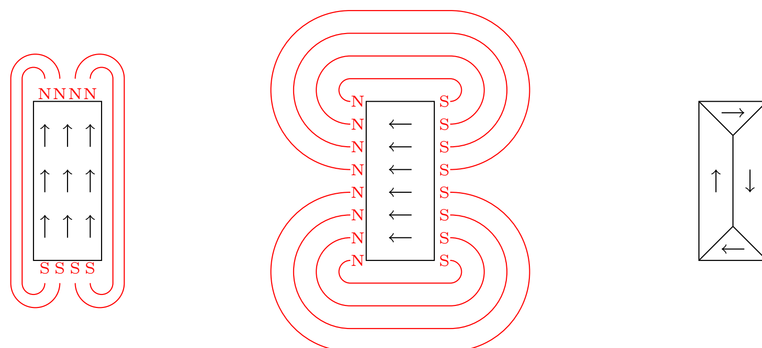


**(a)** Magnetization along easy axis

**(b)** Magnetization along hard axis

**(c)** Flux closure by domain formation

**Figure 2.7:** Illustration of shape anisotropy. Magnetization along the easy axis as shown in **(a)** is more favourable than magnetization along the hard axis, as shown in **(b)**, due a smaller demagnetization field. In **(c)**, domains form a flux closure loop in order to minimize the demagnetization field.

magnetic moments tend to align within the plane of the film, rather than pointing out of plane.

### Magnetocrystalline Anisotropy

Magnetocrystalline anisotropy refers to how easily a material is magnetized along different crystalline axes. In body-centered cubic (bcc) iron, the ⟨100⟩ directions are easy axes, while the ⟨111⟩ directions are hard axes. In face-centered cubic (fcc) nickel, it is the other way around, with the ⟨111⟩ directions being easy axes.

Magnetocrystalline anisotropy stems from the spin-orbit interaction between the spin and orbital motion of electrons, as well as how the the chemical bonds of the orbitals on a given atom are affected by the local crystal field.

### Magnetoelastic Anisotropy

Magnetoelastic anisotropy refers to a change in magnetic susceptibility when a material is subjected to mechanical stress. It is also known as the inverse magnetostrictive effect. Usually, the direction of tensile stress defines the anisotropy direction.

Strain can be induced in a thin film material by lattice mismatch, for instance through epitaxial growth on a lattice-matched substrate, or by field annealing, where the material is annealed in a large magnetic field. After cooling down, the material will be strained.

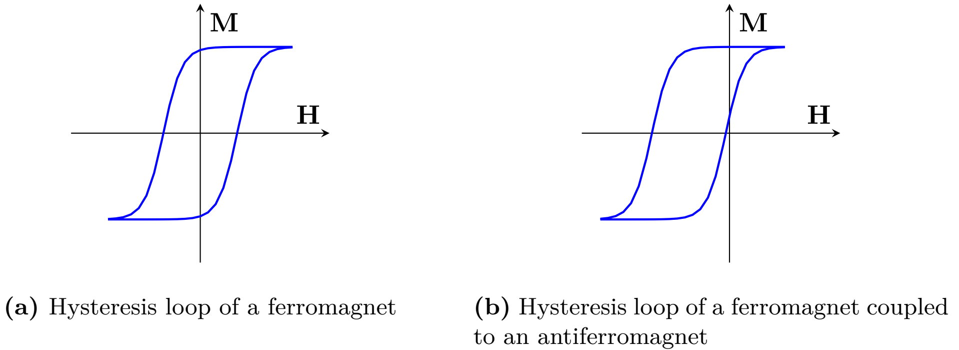


**(a)** Hysteresis loop of a ferromagnet

**(b)** Hysteresis loop of a ferromagnet coupled to an antiferromagnet

**Figure 2.8:** Illustration of the effect of exchange coupling on the magnetization hysteresis loop of a ferromagnetic material coupled to an antiferromagnetic layer.

#### Exchange Anisotropy

Exhange anisotropy, or exchange bias, is a phenomenon in which the hard magnetization behavior of an antiferromagnetic thin film causes a shift in the soft magnetization curve of a ferromagnetic thin film. The exchange bias can be explained by investigating the exchange interaction between the antiferromagnet and the ferromagnet at their interface. Due to the lack of a net magnetization in the antiferromagnet, it is only weakly affected by an external magnetic field. However, at the interface of the antiferromagnet, depending on its crystal orientation, there may be uncompensated spins, such as along the (001) plane of an A-type antiferromagnet, or the (111) plane of a G-type antiferromagnet. Reversal of the interfacial spins of the ferromagnet that are strongly exchange coupled to the antiferromagnet therefore implies an energy cost associated with creating a domain wall, which may shift the magnetization hysteresis curve of the ferromagnet. This is illustrated in Figure 2.8. The exchange coupling may also increase the coercivity of the ferromagnet.

## 2.2 Perovskite Oxides

Perovskite oxides are materials chemically described by the formula $ABO_3$, where B normally is a small cation, while A is a cation of comparable size to the oxygen anion. Many transition metal oxides have the perovskite structure. The ideal perovskite unit cell can be visualized as a cubic lattice of $BO_6$ octahedra with a body-centered A cation, as illustrated in Figure 2.9. Many perovskites have crystal structures that deviate from the ideal cubic lattice, due to different sizes of the A and B cations, as well as the electronic configuration of the octahedral B cation [17]. These distortions include deformation of the oxygen octahedra, cation displacement and rotation of the octahedra.

Several perovskite oxides have been used in this work. STO, with chemical formua $SrTiO_3$, has a cubic perovskite structure. STO is an insulator, and is widely used as a

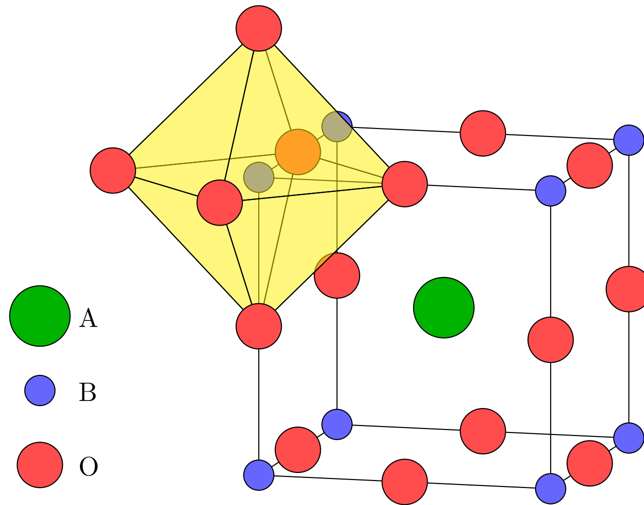


**Figure 2.9:** Ideal perovskite unit cell, with a $BO_6$ octahedron highlighted.

substrate for epitaxial growth of other perovskite oxides due to its favourable lattice parameter $a = 3.905$ Å [18]. By doping with a small amount of niobium (Nb), STO can be made conductive. While pure STO is diamagnetic, doping with Nb concentrations of 0.5 wt% or higher has been reported to make it ferromagnetic [19]. Other perovskite oxides include LSMO and LFO.

### 2.2.1 Lanthanum Strontium Manganite

Manganites are perovskite oxides where the B cation is manganese (Mn), and the A cation is a rare earth or alkaline metal. After the discovery of the colossal magnetoresistive effect in 1994 [20], large interest has been shown for these materials. One such material is LSMO, with chemical formula $La_{1\text{-}x}Sr_xMnO_3$. In LSMO, both lanthanum (La) and strontium (Sr) take the place of the A cation. Since La is trivalent, and Sr is divalent, this directly determines the fraction of the $Mn^{3+}$ and $Mn^{4+}$ oxidation states of manganese. LSMO has been studied extensively for varying values of $x$ [21]. At strontium concentrations $x < 0.1$, the $MnO_6$ octahedra are rotated and tilted in such a way that the Mn–O orbital overlap is small, and the material is an antiferromagnetic insulator. As the Sr doping is increased, the average ionic radius of the A site $r_A$ increases, straightening out the $MnO_6$ octahetra. Above $x = 0.1$, the material becomes ferromagnetic, and at $x > 0.175$, it becomes half metallic. Above $x = 0.5$, the material becomes antiferromagnetic.

**$La_{0.7}Sr_{0.3}MnO_3$**

In this work, a Sr concentration of $x = 0.3$ has been used. $La_{0.7}Sr_{0.3}MnO_3$ is a ferromagnetic half metal, with a Curie temperature $T_C = 370\,K$ [22]. The conductivity as well as the ferromagnetic ordering of $La_{0.7}Sr_{0.3}MnO_3$ can be explained by the double exchange interaction, as described in Section 2.1.2, as well as an electron-phonon interaction known as the Jahn-Teller effect [23]. All further references to LSMO in this work will be to $La_{0.7}Sr_{0.3}MnO_3$.

LSMO has a magnetocrystalline easy axis along the $\langle 111 \rangle$ directions due to the rhombohedral distortion of the unit cell [22]. In (001)-oriented thin films, this would however yield an out-of-plane component of the magnetization. The magnetization therefore falls into the $\langle 110 \rangle$ directions in order to minimize the surface magnetization [24], leading to biaxial anisotropy. The $\langle 100 \rangle$ directions are magnetocrystalline hard axes.

The pseudocubic lattice parameter of LSMO is $a = 3.88\,\text{Å}$. This means that LSMO can easily be epitaxially grown on STO, as the lattice mismatch is minimal. Each manganese atom contributes on average $3.7\,\mu_B$ to the magnetization of LSMO at 0 K [25]. At the LSMO/STO interface, a nonmagnetic layer known as a *magnetic dead layer* has been reported to extend several unit cells into the LSMO layer [26–28]. The manganese atoms in this dead layer do not contribute to the magnetization of the material.

### 2.2.2 Lanthanum Ferrite

LFO is an antiferromagnetic and insulating perovskite oxide with chemical formula $LaFeO_3$. It has an orthorhombic crystal structure. The antiferromagnetic ordering of LFO is due to the superexchange interaction, as described in Section 2.1.2. LFO is a G-type antiferromagnet with a Néel temperature $T_N = 740\,K$ [29].

When grown epitaxially on STO(001) or $LSMO(001)_{pc}$, the LFO unit cell orients itself with the (110) plane parallel to the surface [29]. This means that the spins at the LFO interface are compensated, and the interface has no net magnetization.

### 2.2.3 LFO/LSMO Bilayers

At the interface between a bilayer of LFO and LSMO grown on STO(001), the LFO interfacial layer is magnetically compensated. No exchange bias is therefore expected [30]. However, a microscopic Heisenberg model shows that a perpendicular alignment between the antiferromagnetic and ferromagnetic layers is favored [31]. This alignment is known as *spin-flop coupling*. Recent work has shown that shape anisotropy can break the spin-flop coupling in LFO/LSMO bilayers and cause colinear alignment between the spins of the LFO and LSMO layers [8].

# Chapter 3

# Experimental Methods

*This chapter discusses the experimental methods and approaches used in this project in order to create nanoscale magnetic structures in perovskite thin films. First, an overview is given of the sample preparation process, before the instruments and processes involved are described in more detail. Then, the complete fabrication process is given, followed by an introduction to different techniques of characterization, with emphasis on the VSM, which is used for magnetic characterization.*

## 3.1 Sample Preparation

### 3.1.1 Overview

In this project, we wanted to develop a process capable of creating extended arrays of nanoscale structures defined in perovskite oxide thin films, in order to perform macroscopic measurements of the magnetic properties of such structures. The process development was performed on non-magnetic 0.05 wt% niobium-doped (001)-oriented STO substrates, while magnetic structures were defined in thin films of LFO and LSMO grown by PLD on the same kind of substrate. In this text, *test samples* refer to the bare Nb:STO substrates, while *thin film samples* refer to samples where films consisting of LFO on top of LSMO were grown on the Nb:STO substrates. Several test samples were used, while a single thin film sample was eventually processed.

In order to be able to perform macroscopic measurements of the properties of nanostructures, an area of comparable size to the entire surface of the sample must be patterned. SCIL has been employed in order to fulfill this requirement, as it is a technique showing great promise for uniform patterning of structures over large areas. Section 3.1.2 describes the SCIL process in detail. Inductively-coupled plasma reactive ion etching (ICP-RIE) was used to etch the residual layer that is left after performing any kind of nanoimprint lithography, including SCIL. ICP-RIE is described in detail in Section 3.1.3. Finally, using the nanoimprint resist as a mask, ion implantation was used in order to disrupt the magnetic order of the exposed areas, leaving magnetic nanostructures with shape defined by the nanoimprint resist mask. Figure 3.1 illustrates the process flow.

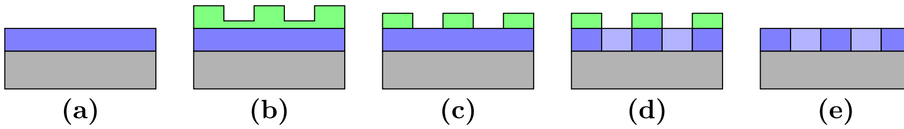


**Figure 3.1:** Overview of process flow. **(a)** A magnetic thin film (blue) is grown on a substrate (gray). **(b)** A resist layer (green) is patterned using SCIL. **(c)** The residual layer of resist is etched. **(d)** The magnetic order of parts of the thin film (light blue) is disrupted by ion implantation. **(e)** The resist is removed, leaving embedded nanoscale magnets (dark blue) in a non-magnetic matrix.

### 3.1.2 Substrate Conformal Imprint Lithography

NIL is a lithographic technique that works by replicating a master pattern in a resist layer using a stamping process. As such, it differs fundamentally from other common lithographic techniques, like photolithography and EBL, which use energetic particles to change the chemical properties of parts of the resist layer. In the NIL process, the resist layer is molded to obtain the inverse shape of the master stamp. Master stamps can be fabricated using EBL or interference lithography. After creating a master, it can be re-used multiple times.

The first NIL processes were known as thermoplastic nanoimprint lithography (T-NIL) and made use of the fact that the viscosity of a thermoplastic polymer is strongly reduced above the glass transition temprature, $T_g$. This allows for stamping a pattern into a heated polymer, before allowing the polymer to cool in the desired shape. Further improvements include UV-cured nanoimprint lithography (UV-NIL), in which a UV-curable polymer resist and a transparent stamp is used. This reduces the pressure required to press the stamp into the resist compared to T-NIL [32]. A third imprint-based technique is known as soft lithography. In this technique, a soft stamp, typically made from a silicone elastomer such as poly(dimethylsiloxane) (PDMS) is used instead of a rigid stamp. However, soft lithography is unsuitable for nanoscale patterns, as the nanoscale features of the stamp are too flexible, causing them to collapse under the influence of surface tension [33]. A more detailed account of different NIL techniques, along with their advantages and disadvantages, has been given by Mellbye [11].

SCIL is a method developed by Philips Research and SUSS MicroTec in order to improve on some of the issues with standard UV-NIL using a hard stamp, utilizing some of the advantages of soft lithography [34].

#### Operational Principle of SCIL

As described by Verschuuren [35], a stamp consisting of multiple layers is used in the SCIL process. Two elastomer layers are fixed on a thin glass support. The pattern to be imprinted is molded in the outer elastomer layer, which typically is made from a stiff silicone elastomer called hard-PDMS. Like normal PDMS, hard-PDMS can be produced by mixing a base and a curing agent in the correct ratio. The base used to

mix hard-PDMS is a proprietary mixture of two vinyl elastomers. Hard-PDMS has an elastic modulus of $8 - 12$ MPa, compared to $2 - 3$ MPa for commercial Sylgard 184 PDMS. The hard-PDMS layer is typically approx. 100 µm thick. The second elastomer layer is an approximately $500 - 1000$ µm thick cushion of PDMS, which also serves as a glue between the glass and the hard-PDMS. A rubber frame is affixed to the glass in order to improve the stability and to create a vacuum seal between the stamp and the stamp holder when imprinting. Figure 3.2 illustrates a complete SCIL stamp.

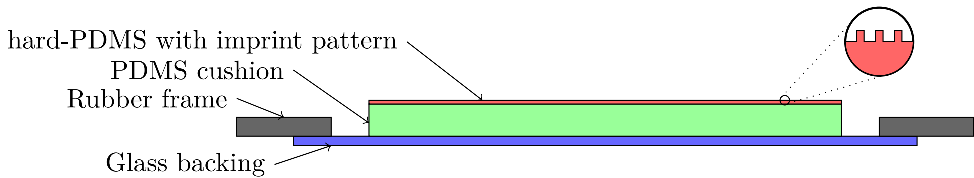


**Figure 3.2:** Illustration showing the components of a SCIL stamp, including the glass backing, rubber frame, PDMS intermediate layer and hard-PDMS patterned layer.

The SCIL stamp is fitted on a stamp holder which contains multiple grooves, and is held in place by vacuum. A substrate coated with a UV-curable resist layer is placed below the stamp, with a process gap of $50 - 150$ µm between the substrate and the stamp. The stamping process is initialized by pressurizing the grooves of the stamp holder sequentially. An overpressure of approximately 2 kPa of nitrogen is applied to each groove, making the stamp bulge and come in contact with the resist. The stamp is pulled into the resist by capillary force, rather than being pushed by the applied nitrogen pressure. The grooves are pressurized in sequence, putting the stamp in contact with the resist in a rolling motion. After UV exposure and hardening, the stamp is removed by sequentially evacuating the grooves, releasing the stamp with the same rolling motion as was used to perform the imprinting. Figure 3.3 shows a schematic of the SCIL imprinting principle.

The SCIL technology has multiple advantages over nanoimprint processes using rigid stamps. Due to the flexible nature of the SCIL stamp in the out-of-plane direction, conformal contact can be made over large areas. The stamp is also able to deform around particle contaminants on the substrate. At the same time, the glass backing and hard-PDMS layers prevent distortion of the pattern in the in-plane directions, ensuring reliable pattern replication. Air bubbles that are trapped between the stamp and the substrate may escape by diffusing through the stamp, as PDMS has a high permeability for gases. The flexibility of the stamp also aids the release process, as the silicone elastomer temporarily deforms on release. This makes it possible to imprint features with high aspect ratio. The use of an anti-stick coating on the stamp is not required, due to the low surface energy of PDMS.

Several parameters have to be controlled when performing SCIL. In order to produce imprints without air bubbles being trapped between the stamp and the substrate, the pitch and width of the grooves in the stamp holder is important. This parameter is however dictated by the manufacturer of the stamp holder. The step time between

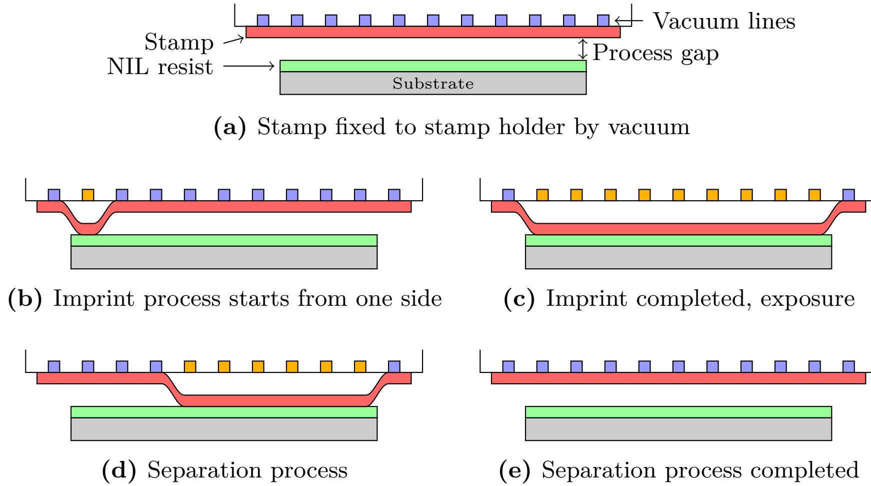


**(a)** Stamp fixed to stamp holder by vacuum

**(b)** Imprint process starts from one side

**(c)** Imprint completed, exposure

**(d)** Separation process

**(e)** Separation process completed

**Figure 3.3:** SCIL imprint and separation sequences.

flushing each groove with nitrogen is also important, as this regulates whether the resist has sufficient time to flow into the pattern before the next groove is pressurized. By allowing the resist to flow before proceeding to the next groove, better filling of the stamp features is ensured. After pressing the stamp and substrate together, a process delay may be required in order to allow the remaining resist to flow and settle, before exposing. A sufficient exposure dose at the correct wavelength is necessary to cure the resist. After exposure, a post-process delay may be allowed for in order to completely cure the resist before separation is initialized.

Another parameter which is important with SCIL, as well as with other imprint lithography techniques, is the thickness of the residual resist layer after imprinting [36]. The residual layer thickness depends on the structure density and structure height, as well as on the initial resist thickness before imprint. The residual layer thickness can be calculated by the formula

$$R = T - H \cdot \frac{N}{P + N} \tag{3.1}$$

where $R$ is the residual layer thickness, $T$ is the initial resist thickness, $H$ is the height of the imprinted structure, and $P$ and $N$ are the area fractions of positive and negative structures on the stamp, respectively. In an optimized nanoimprint process, the residual layer is as thin as possible.

### Nanoimprint Stamp Replication

A four-inch silicon wafer containing four areas of nanoscale line patterns of different pitch was obtained from Eulitha AG. Each area had a size of $10 \times 10\,\mathrm{mm}^2$, and the pitch of the line patterns were 300 nm, 400 nm, 500 nm, and 600 nm, respectively. All line patterns were specified to have a positive area fraction of 50 %, i.e. that the width

of the lines was equal to the space between the lines. The height of the features was specified to be approx. 210 nm. The layout and dimensions of the wafer are shown in Figure 3.4.

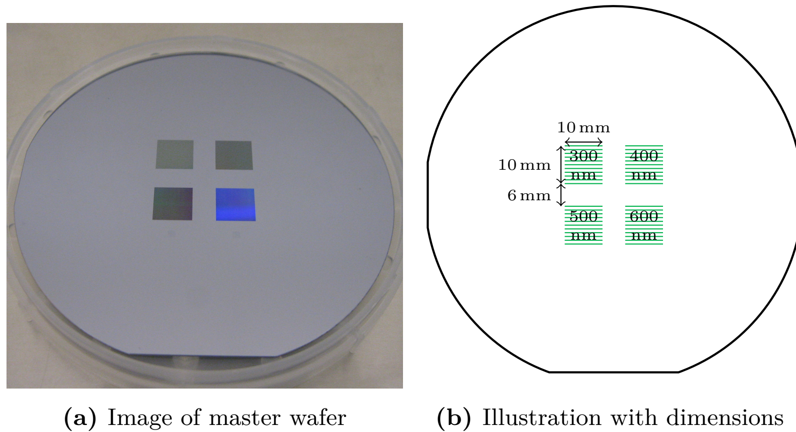


**(a)** Image of master wafer **(b)** Illustration with dimensions

**Figure 3.4:** 4-inch (100 mm) Eulitha silicon master wafer

Two SCIL stamps having the inverted line pattern of the master wafer were manufactured by mixing and applying hard-PDMS to the master wafer using a Laurell Technologies spin coater. The master was then loaded into a SUSS master replication tool (MRT), along with a 200 µm thick $200 \times 200\,\text{mm}^2$ glass plate that had previously been etched in a 1 % HF solution in order to remove microcracks along the edges. Ordinary PDMS was mixed and poured onto the master, before the glass was placed in contact with the PDMS, and the PDMS was spread using the micrometer screws of the MRT.

After curing at 50 °C for 24 h in the MRT, the wafer with PDMS and glass backing was moved to a drying oven to cure for 96 h at 50 °C. After curing, a rubber frame was glued onto the edges of the glass backing using an epoxy resin. Any overrun of PDMS was cut away from the edges of the master wafer using a scalpel. Ethanol was used for lubrication while cutting away the PDMS overrun.

Since the master wafer was only patterned in the center, there was little adhesion between the master and the hard-PDMS along the edges. The wafer therefore easily separated from the SCIL stamp without using a SUSS peel-off tool (POT). The stamp was cleaned with ethanol, and stored in a nitrogen cabinet for 24 h before use. Figure 3.5 shows a completed stamp. Details of the SCIL stamp replication process have been given previously by Mellbye [11].

After allowing the SCIL stamps to cure in a nitrogen cabinet, they were optically inspected. The nanoscale pattern of the first stamp was investigated using a Hitachi S-5500 scanning electron microscope (SEM). The glass backing was cut using a diamond-tip scribing tool, and the PDMS was cut using a scalpel, to obtain a small piece of the stamp, with glass backing, PDMS and hard-PDMS layers. The piece of the stamp

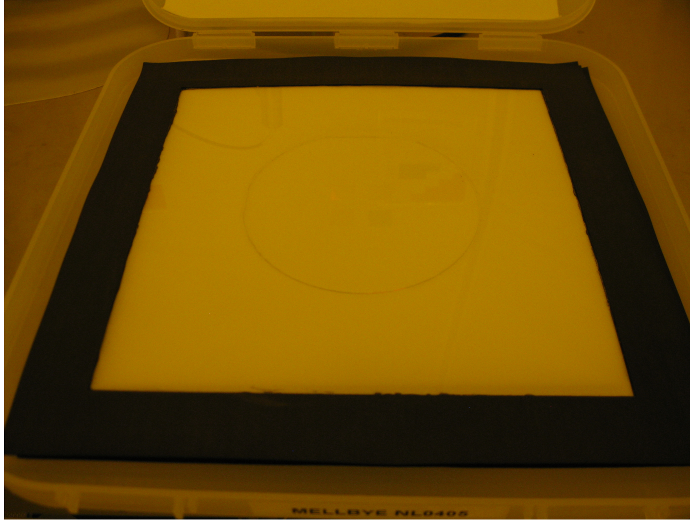

**Figure 3.5:** Complete SCIL stamp with rubber frame and glass backing

was mounted on a SEM sample stub, and 5 nm of a platinum-palladium alloy was deposited using a Cressington 208R sputter coater. This was done to make the stamp conductive, in order to reduce charging effects in the SEM.

### SCIL Wafer Chuck Adapter

In order to perform SCIL on small samples with a SUSS MA6 mask aligner, an adapter was needed in order to fit the $7.5 \times 7.5\,\mathrm{mm}^2$ STO samples in the 2-inch SCIL wafer chuck of the mask aligner. The MA6 mask aligner performs a wedge error compensation (WEC) step before imprinting, in order to ensure that the chuck is at the correct angle and distance from the SCIL stamp before loading the sample. In contact aligning mode, WEC is performed with the sample in place. However, when performing SCIL, the resist on the sample should not make contact with the stamp before the imprinting routine starts. A dummy sample can therefore be used for WEC. It is important that the surface of the wafer chuck is as flat as possible and at the correct height. As such, the adapter needed to have a uniform thickness, and have a precisely machined hole for holding the sample.

**Adapter Tolerances** In order to ascertain the tolerances for the thickness of a SCIL adapter, back-of-the-envelope calculations were performed to find how much the stamp would be able to bend and compress in order to make contact with a sample situated too low relative to the adapter.

The 200 µm glass backing of the stamp can be modelled as a thin membrane, fixed to the edges of the 7.5 mm sample hole. As given by Liu [37], the formula for the maximum displacement of a membrane of dimensions $a \times b$ under uniform pressure $p$

is

$$w_{center} = \frac{\alpha p b^4}{E t^3} \tag{3.2}$$

where $\alpha$ is determined by the ratio between $a$ and $b$. For $a = b = 7.5\,\mathrm{mm}$, $\alpha = 0.0138$. The elastic modulus $E$ of the glass plate is $E \approx 50\,\mathrm{GPa}$ [38], and the thickness $t = 200\,\mu\mathrm{m}$. The applied pressure is typically $p = 2\,\mathrm{kPa}$ for SCIL [35]. This gives a total displacement at the center of the glass of $w_{center} = 218\,\mathrm{nm}$.

In addition to causing the glass to flex, the applied overpressure of nitrogen will cause the PDMS cushion to be compressed. Assuming that the part of the stamp over the sample hole is unaffected, while the parts in contact with the adapter are compressed, the ability of the PDMS to fill the hole can be estimated. From Hooke's law [39], we have that

$$\varepsilon = \frac{p}{E} \tag{3.3}$$

where $\varepsilon$ is the strain of the material. Using $p = 2\,\mathrm{kPa}$, $E = 2\,\mathrm{MPa}$, and the definition of the engineering strain, the change in thickness will be $0.001 \cdot t_0$, where $t_0$ is the initial thickness. For a $600\,\mu\mathrm{m}$ PDMS cushion, the change in thickness will be $600\,\mathrm{nm}$. The hard-PDMS, with $E = 12\,\mathrm{MPa}$ [35], will see a thickness change of approximately $30\,\mathrm{nm}$.

From this, it is clear that the stamp will not be able to compensate for situations where the sample is situated more than approximately $1\,\mu\mathrm{m}$ too deep in the adapter. This means that near-perfect alignment of the sample and the adapter is necessary, and that any inaccuracies in the fabrication of the adapter should be accounted for by fabricating an adapter that is too shallow rather than too deep.

**Blind Hole Adapters** Previously, we have achieved successful imprints using a 2-inch wide, $2\,\mathrm{mm}$ thick polycarbonate disk with a $500\,\mu\mathrm{m}$ deep, $7.5 \times 7.5\,\mathrm{mm}^2$ blind hole in the center for holding the sample [11]. A smaller through hole was drilled through the center, and vacuum lines were machined on the backside of the disk in order to connect the sample to the vacuum of the chuck. This design can be seen in Figure 3.7a. Figure 3.6 shows the working principle of the adapter mounted in the wafer chuck.

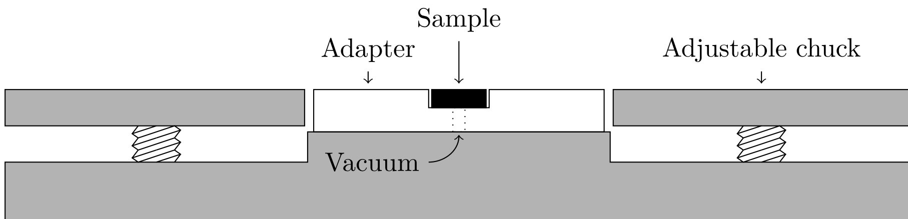


**Figure 3.6:** Cross-section illustration of polycarbonate adapter mounted in wafer chuck

A variation on this design was manufactured by the workshop at the NTNU Department of Electronics and Telecommunication, where the hole for the sample was offset by 7 mm from the center of the disk, in order to line up with the features of the SCIL stamp. The thickness of the polycarbonate disk was also reduced to 1.5 mm in order to provide more leeway on the micrometer adjustment screws on the wafer chuck, as the 2 mm thick adapter only barely fit within the range of the screws. The off-center design is illustrated in Figure 3.7b. An adapter with four holes for samples, as illustrated in Figure 3.7c, was also manufactured.

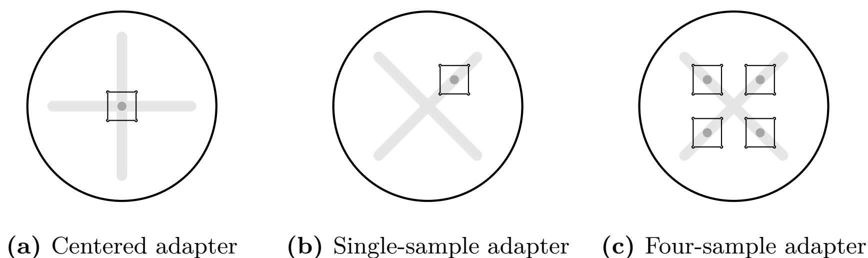

**(a)** Centered adapter **(b)** Single-sample adapter **(c)** Four-sample adapter

**Figure 3.7:** Polycarbonate adapter designs

A polycarbonate adapter was also produced by the workshop at the NTNU Faculty of Natural Sciences and Technology. In this design, the vacuum lines on the backside of the adapter were omitted. Figure 3.8 shows the adapter with a sample mounted. The backside is covered with blue tape in order to improve vacuum contact.

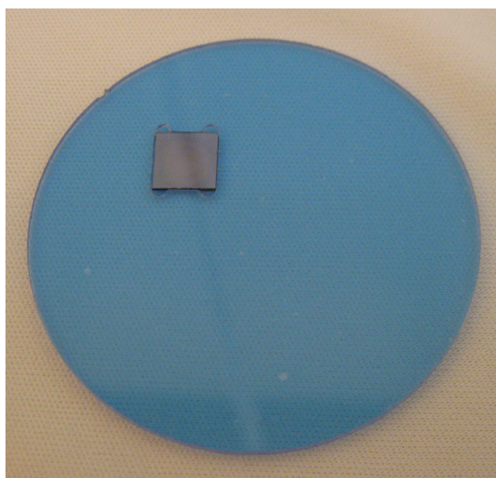

**Figure 3.8:** SCIL adapter with sample and blue tape on backside

**Through Hole Adapters** A different approach was also taken to create an adapter for the wafer chuck. A potential issue with the polycarbonate adapter was that it did not utilize the three-point sample leveling mechanism of the SCIL wafer chuck, meaning that it would have to be machined perfectly within the $< 1\,\mu\text{m}$ tolerance calculated previously. By using a large, flat surface with a through hole for the sample, the adapter would move with the adjustable perimeter of the wafer chuck, while the sample would have a fixed height. Figure 3.9 illustrates the working principle for such an adapter.

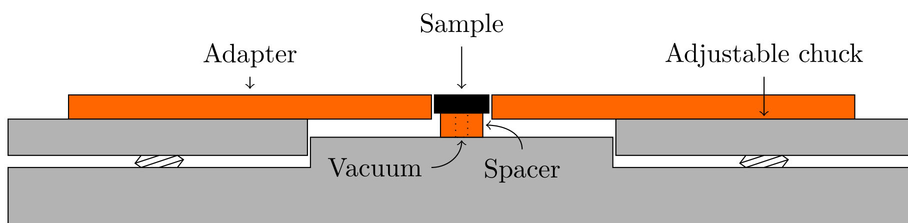


**Figure 3.9:** Cross-section illustration of through hole adapter mounted on the wafer chuck

A $120 \times 120\,\text{mm}^2$ stainless steel plate with a thickness of $300\,\mu\text{m}$, and a laser-cut $7.6 \times 7.6\,\text{mm}^2$ hole in the center was ordered from a commercial company. The stainless steel plate was chosen to be thinner than the samples, in order to make it possible to use the adapter without utilizing a spacer underneath the sample, as illustrated in Figure 3.9.

A similar adapter was produced by the workshop of the NTNU Department of Electronics and Telecommunications from a 1.5 mm thick copper-coated FR-4 circuit board. A $7 \times 7\,\text{mm}$ square spacer with a 3 mm hole in the center was fabricated from the same material. The various SCIL adapters were tested on the SUSS MA6 mask aligner.

### 3.1.3 Reactive Ion Etching

As described by Quirk & Serda [40] and by Welch [41], reactive ion etching (RIE) is a dry etching technique commonly used in microfabrication. Using a chemically reactive plasma, material is removed from the sample by physical and chemical means. The plasma is generated in a vacuum by an electromagnetic field, and the ions from the plasma are accelerated towards the wafer, where they attack the wafer surface.

Due to the sample being electrically isolated, electrons from the plasma build up on the sample, giving it a negative DC bias. This leads to ions being accelerated towards the sample, where they remove material by a combination of sputtering and chemical reactions.

The most important parameters for a good etching process include the etch rate and selectivity between materials, the etch profile and etch bias, and the uniformity

of the etch across the sample and between multiple sample batches. In RIE, the etch profile is usually anisotropic. When etching small structures, good control of the etching parameters is important in order to etch high aspect ratio features with good control of the critical dimension.

When etching different materials, different etchant gases are used. For etching oxides such as $SiO_2$, fluorocarbon chemistry is normally used. Common etchants include $CF_4$ and $CHF_3$. Silicon is often etched using chlorine or bromine chemistry, using gases such as $Cl_2$, $BCl_3$ or HBr. $SF_6$ can also be used. Metals are also etched using chlorine chemistry. Inert gases such as Ar or He are often added to the etch chemistry to increase the physical action of the etch or to dilute the reactive gas to enhance plasma uniformity.

Since dry etching processes usually have a relatively poor selectivity to the underlying layer, a form of *endpoint detection* should be used to monitor the etch process and minimize overetching of the underlying layer. Endpoint detection systems can use different parameters, including the type of etch products removed from the process, a change in the active reactants in the gas discharge, or a change in the etch rate. One way of measuring the etch rate, is using a laser interferometer. When etching a partially reflecting layer, the reflected light will interfere constructively or destructively with the incident light depending on the thickness of the layer, modulating the intensity of the detected signal. This can be used to automatically stop the etch when the layer has been etched through.

#### Inductively Coupled Plasma RIE

In an ICP-RIE etcher, the production of the plasma is decoupled from the sample. This allows for generating a higher-density plasma at a lower pressure. A high-density plasma is able to enter and exit high aspect ratio features, which is necessary in order to etch structures on the nanoscale.

The ICP-RIE etcher generates plasma using RF power applied to a spiral coil, which is electrostatically shielded from the plasma. This ensures a purely inductive coupling. In addition, another RF source is used to direct the plasma towards the sample.

Figure 3.10 shows an illustration of an ICP-RIE setup. The sample is situated at the bottom of the chamber, electrically isolated from the rest of the chamber. Precursor gases, regulated by a mass-flow controller, are injected through the top of the chamber. The gas pressure is typically maintained in the range $0.1 - 100\,\mathrm{mTorr}$.

### 3.1.4 Ion Implantation

Ion implantation is a physical process for introducing controlled amounts of dopants into a substrate [40]. The main application of ion implantation is the doping of semiconductor materials. An ion implanter has an ion source that creates dopant ions from a source material. Using a mass analyzer, the ions are separated to create a beam of the desired ions. The ion beam is accelerated by an electric field to attain the desired kinetic energy. The beam scans the substrate to provide a uniform distribution

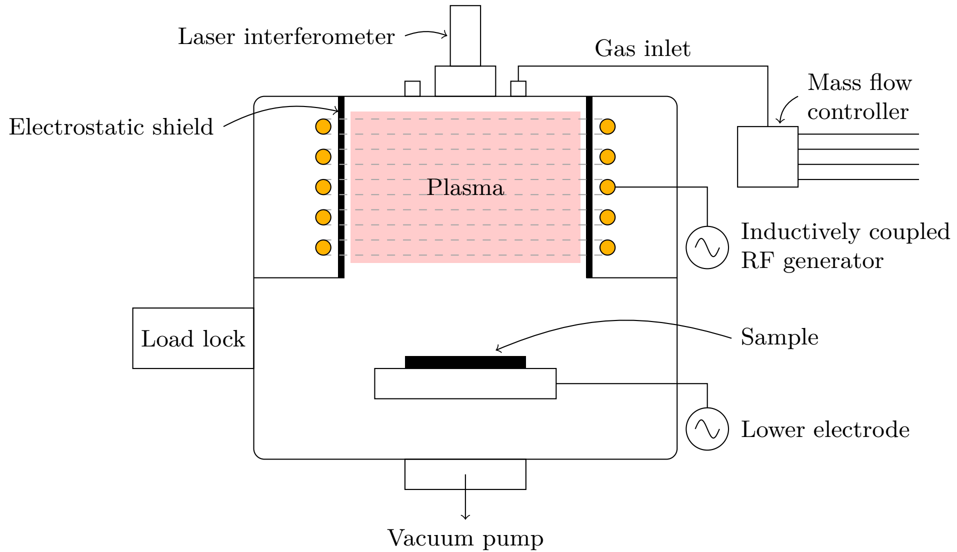


**Figure 3.10:** Schematic of an ICP-RIE tool

of dopant ions. The implantation process is usually followed by a thermal annealing step.

The two most important ion implant parameters are the *dose* $Q$, describing how many ions are implanted per square centimeter, and the *projected range* $R_p$, which describes how deep the ions travel into the substrate. The spread in depth of the ions around $R_p$ is known as *straggle*, $\Delta R_p$.

### $Ar^+$ Implantation in Perovskite Thin Films

As shown by Takamura *et al.* [5] and Folven *et al.* [6], the magnetic properties of thin films of LSMO and LFO can be modified by implantation of $Ar^+$ ions. Using a dose of approximately $1 \cdot 10^{14}/\mathrm{cm}^2$, the crystal lattice is distorted. Since the superexchange and double exchange mechanisms for antiferromagnetism and ferromagnetism in the perovskite oxides are sensitive to the orbital overlap between the magnetic cation and the oxygen anion, this leads to the materials losing their permanent magnetization, and becoming paramagnetic.

## 3.1.5 Process Recipe

Amonil MMS4 resist from AMO GmbH was chosen as the UV nanoimprint resist. It has a low viscosity of 50 mPa s [42]. The low viscosity makes it suitable for SCIL, as the imprint pressure is low, and the wetting of the SCIL stamp is driven by capillary forces [35]. Amonil requires a dose of $5000\,\mathrm{mJ/cm}^2$ at 320 nm in order to fully cure. Amonil is a composite material, consisting of organic compounds, as well as inorganic

silica-based compounds. This combination makes it a hard resist that is difficult to remove from the substrate after processing [43]. In order to facilitate the removal of the Amonil resist after ion implantation, a thin underlayer of PMMA from MicroChem with a molecular weight of 950K was added. PMMA is a deep UV (DUV) and electron beam resist, and PMMA is easily removed in acetone [44].

Based on a Stopping and Range of Ions in Matter (SRIM) simulation performed previously [11], an Amonil resist thickness of 130 nm was estimated to suffice as a mask for argon ion implantation. The features of the SCIL stamp, with a height of 210 nm, were therefore considered to be sufficient to create an Amonil mask for ion implantation.

#### Process Development

SCIL and ICP-RIE process parameters were based on recipes that had previously been found to work [11]. Several test samples were used in order to optimize the residual layer thickness of the Amonil resist after imprinting. This was done by varying the rotational speed for the spin coating of Amonil onto the sample. No PMMA underlayer was used for residual layer thickness optimization. Test samples were also used to optimize the etching time, as the geometry of the resist pattern precluded optical endpoint detection.

#### Sample Preparation Process

This section lists the entire sample preparation process for the thin film samples. Test samples were prepared using the same process, except for the thin film deposition and characterization, as well as the ion implantation.

**Sample cutting** 0.05 wt% niobium-doped STO substrates with a size of $15 \times 15\,\text{mm}^2$ were cut into four equal pieces of $7.5 \times 7.5\,\text{mm}^2$ using a Struers Minitom cut-off machine with a diamond blade, a cutting pressure of 75 g, and a rotation speed of 100 rpm.

**Pre-deposition sample clean** In order to ensure a clean and smooth surface for epitaxial growth of thin films, samples were cleaned using acetone followed by ethanol, and blown dry using nitrogen gas.

**Thin film deposition** Thin films of LFO and LSMO were grown using the PLD system at the NTNU Department of Electronics and Telecommunications in accordance with standard procedure [7]. A bilayer thin film of approximately 10 unit cells LFO on top of 90 unit cells LSMO was grown on sample P50319. *(The film growth was performed by Fredrik K. Olsen.)*

**Thin film characterization** After thin film growth, the film was characterized using a Veeco MultimodeV atomic force microscope (AFM). *(This characterization was performed by Fredrik K. Olsen.)*

**Sample clean** During thin film deposition, the substrates were glued to a sample holder using silver glue. This residual glue layer was removed from the samples by placing the sample upside down on a stack of several cleanroom wipes, and gently scraping off the residual glue using a scalpel.

Samples were cleaned by ultrasonication in acetone for 5 min, followed by flushing with ethanol in order to prevent the acetone from drying on the surface. The samples were then blown dry using nitrogen gas.

**Dehydration bake** In order to drive out excess moisture, samples were baked at 95 °C on a hotplate for 5 min.

**Spin coating** An approximately 50 nm thick layer of 950K PMMA A2 from MicroChem was spin-coated on the samples at 5000 rpm for 45 s with an initial acceleration of 1000 rpm/s. The samples were then pre-baked for 60 s at 180 °C on a hotplate. After cooling on a coolplate, Amonil MMS4 was applied by spin coating at 5000 rpm for 30 s with an initial acceleration of 4000 rpm/s, giving an Amonil resist layer of approximately 150 nm.

**Substrate conformal imprint lithography** Before imprinting, a SUSS UV optometer was used to measure the intensity of the UV light of the SUSS MA6 mask aligner at 320 nm. From this, the exposure time necessary to achieve the required exposure dose was calculated. An adapter, as described in Section 3.1.2, was mounted in the SCIL wafer chuck, and a WEC step was performed. The adapter was aligned with the desired pattern in the SCIL stamp. The sample was then mounted in the adapter. Table 3.1 lists the parameters used for imprinting. Appendix A contains detailed instructions for using the SUSS MA6 mask aligner at NTNU NanoLab for SCIL.

**Table 3.1:** Process parameters for SCIL imprinting

| **Parameter** | **Value** |
|---|---|
| Imprint pressure | 1.7 kPa |
| Process gap | 50 µm |
| Imprint area | 100 mm |
| Step time imprint | 3.0 s |
| Process delay | 240 s |
| Exposure dose | 5000 mJ/cm$^2$ |
| Post process delay | 180 s |
| Step time separation | 3.0 s |

After imprinting, the samples were optically inspected using a Nikon SMZ460 stereomicroscope, as well as a Nikon Eclipse LV150 yellow light microscope.

**Residual layer etch** The residual layer of Amonil and PMMA was etched using ICP-RIE in an Oxford Plasmalab System 100 with an ICP180 source electrode. Ta-

ble 3.2 lists the parameters used for residual layer etch.

**Table 3.2:** Process parameters for ICP-RIE etch

| Parameter | Value |
|---|---|
| Gas flows | $CF_4$: 15 sccm |
| | $CHF_3$: 15 sccm |
| Chamber pressure | 5 mTorr |
| RF power | 75 W |
| ICP power | 25 W |
| Etch time | 110 s |

After residual layer etching, the samples were optically inspected using a Nikon SMZ460 stereomicroscope, as well as a Nikon Eclipse LV150 yellow light microscope.

**Ion implantation** Thin film samples were implanted using $Ar^+$ ions at Innovion Corporation, San Jose. Ions were accelerated to 50 keV, and a dose $Q \approx 1 \cdot 10^{14}/\text{cm}^2$ was implanted in order to disrupt the magnetic order in the exposed areas of the thin film.

**Resist removal** After ion implantation, samples were sonicated in acetone for 5 min in order to dissolve the PMMA and lift off the Amonil. However, this was found to be insufficient to remove all of the resist. An acetone airbrush was used to remove residue that did not come off in the ultrasonic bath. Some residual resist was still found to be left on the sample surface. A 60 s etch in glacial acetic acid was therefore employed, as acetic acid is known to dissolve PMMA [45]. The samples were then flushed with ethanol, and blown dry using nitrogen gas.

## 3.2 Characterization

### 3.2.1 Overview

The finished thin film sample, designated P50319, was characterized using an AFM, which is described in Section 3.2.2. Hysteresis curves and measurements of magnetic moment vs. temperature were performed using a VSM. Section 3.2.3 describes the VSM and magnetic measurement system in further detail.

### 3.2.2 Scanning Probe Microscopy

#### Atomic Force Microscope

The atomic force microscope is based on measuring the attractive or repulsive forces between a tip and the sample surface. The AFM tip is mounted on a flexible cantilever. The forces cause the cantilever beam to deflect, and the deflection is optically detected by a photodiode. The signal is translated to represent the topographical features of the surface. By raster scanning the tip across the surface, a 3D map of the surface

structure can be generated. Unlike the scanning tunneling microscope (STM), the AFM works with any material, including insulating samples. The AFM is able to operate in both air and liquid. Figure 3.11 illustrates the working principle of an AFM.

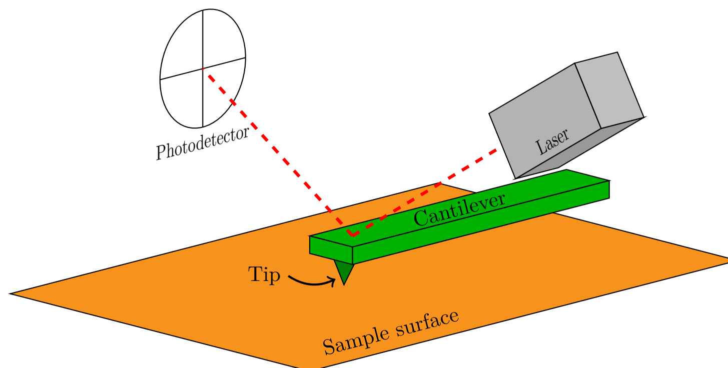


**Figure 3.11:** Illustration of an AFM.

AFMs may be operated in several different modes [32]. In *contact mode*, the tip is moved along the surface, and deflection of the tip is detected. In *tapping mode*, the cantilever is driven to oscillate at or near its resonance frequency, and modulation of the oscillation amplitude is detected. In *noncontact mode*, the tip is oscillating out of contact with the sample, and modulation of the oscillation frequency or phase is detected.

#### Surface Characterization

A Veeco MultimodeV AFM was used to image the surface of sample P50319 after processing. Images were taken in tapping mode, using a Bruker TESP AFM tip.

### 3.2.3 Vibrating Sample Magnetometer

#### Operational Principle

The VSM is an instrument used for measuring the magnetic moment of a sample in an applied uniform magnetic field with high sensitivity. From this, magnetic properties as a function of temperature and applied field can be measured. The VSM was first described by Foner [46].

A VSM works by vibrating the sample relative to a uniform magnetic field, typically using a piezoelectric transducer element. The dipole field of the oscillating sample is picked up by a set of stationary detection coils. The magnetic moment of the sample can be deduced from the voltage induced in the detection coils, which according to Faraday's law is given by

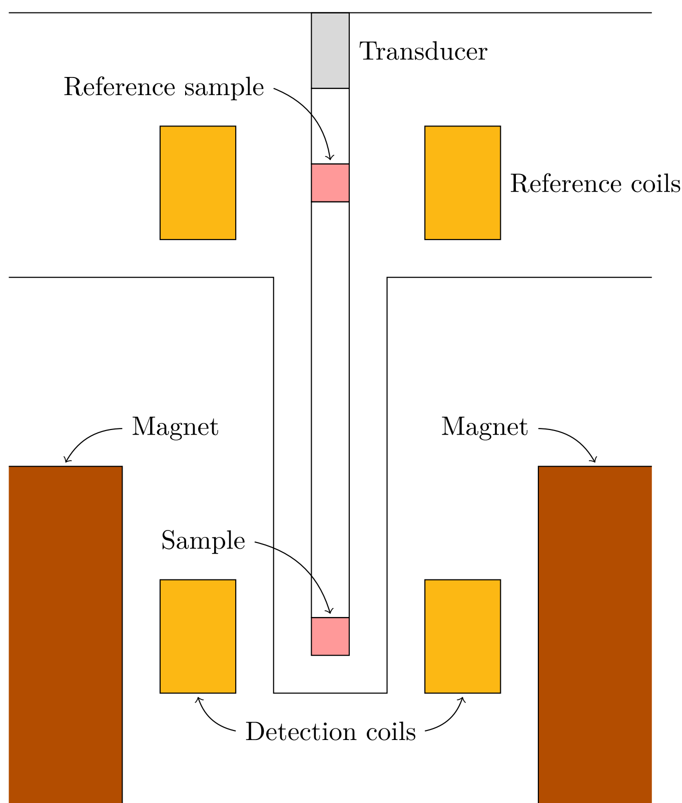


**Figure 3.12:** Schematic of a vibrating sample magnetometer

$$\mathcal{E} = -\frac{\partial \Phi}{\partial t} = -\frac{\partial \Phi}{\partial z}\frac{\partial z}{\partial t} \tag{3.4}$$

A reference sample can be used to make the measurement insensitive to changes in the vibration amplitude and vibration frequency, as well as nonuniformities in the applied magnetic field. The design of the detection coils is also essential for minimizing background noise. Using gradient coils, spatial encoding of the signal is possible. Figure 3.12 shows the general principle of a VSM as described by Foner.

### Magnetic Characterization

Using a Quantum Design VersaLab with VSM module, measurements of magnetic properties were performed for sample P50319. All measurements were performed using a 40 Hz vibration frequency and a 2 mm vibration amplitude in a helium ambient at a chamber pressure of $35 - 70$ Torr.

**Sample preparation** In order to fit the sample on the VSM sample holder, it was cut using a Struers Minitom cut-off machine. A piece from the patterned area of the sample, measuring approximately $4 \times 4\,\mathrm{mm}^2$, was used. In order to be able to scale the measured magnetic moment to the volume of the sample, the surface area was measured by imaging the sample next to a ruler, and analyzing the dimensions using ImageJ[1]. Figure 3.13 shows how ImageJ was utilized to calculate the area of the sample. From this, an area of $A = 16.08\,\mathrm{mm}^2$ was measured.

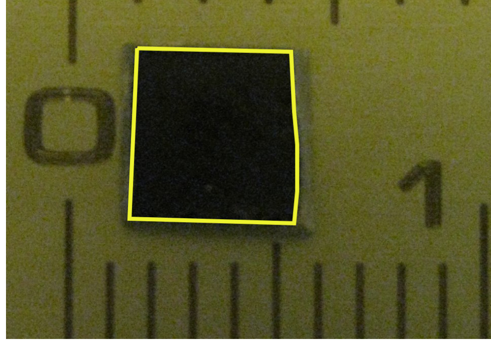


**Figure 3.13:** Sample P50319 with outline for area measurement drawn in ImageJ

The sample area was used, together with the LSMO film thickness and lattice parameter of LSMO, to convert the measurement of the total magnetic moment from the VSM to the magnetic moment per manganese atom according to the formula

$$\mu = \frac{M}{\mu_B} \cdot \frac{a^2}{N \cdot A} \tag{3.5}$$

where $M$ is the total magnetic moment, $\mu_B$ is the Bohr magneton, $a = 3.88\,\text{Å}$ is the pseudocubic lattice parameter of LSMO, $N = 90$ is the thickness of the LSMO thin film given in number of unit cells, and $A = \frac{160\,\mathrm{nm}}{400\,\mathrm{nm}} \cdot 16.08\,\mathrm{mm}^2 = 6.43\,\mathrm{mm}^2$ is the ferromagnetic area of the sample.

The samples were glued onto the VSM quartz sample holder using a gum resin (GE Varnish), and inserted into the VSM chamber. The chamber was purged with He gas and sealed. In order to ascertain the magnetic field necessary to reach magnetic saturation, hysteresis curves, i.e. measurements of the magnetic moment as a function of applied field, were obtained at 300 K and 50 K for two sample orientations, with the uniform magnetic field applied in parallel with the nanoscale line pattern along the [100] axis, and perpendicular to this direction, i.e. along the [010] axis, as illustrated in Figure 3.14, between −10 kOe and 10 kOe.

Using helium cooling, the magnetic moment was continuously measured from 70 K to 400 K. The sample was cooled in zero field, before the saturation moment was measured parallel with the lines with an applied field of 5 kOe for the duration of the temperature sweep. The process was then repeated perpendicular to the lines.

[1] http://imagej.nih.gov/ij/

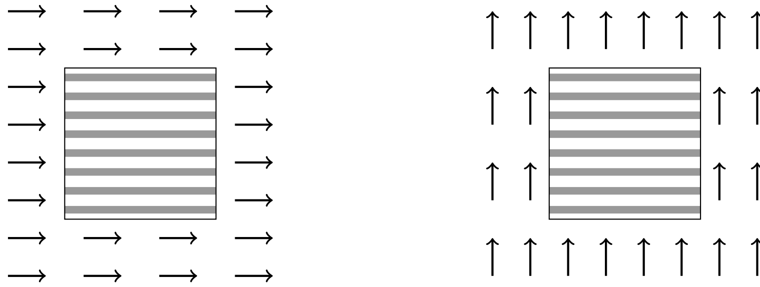

**(a)** Field along [100], parallel with lines **(b)** Field along [010], perpendicular to lines

**Figure 3.14:** Magnetic field **H** applied to the sample in different orientations

Hysteresis curves were obtained in both sample orientations by sweeping the applied magnetic field between −5 kOe and 5 kOe at constant temperature in 25 K intervals from 50 K to 350 K.

**Control sample** Sample P50319 was only partially imprinted, so a small piece from the unpatterned area was used as a control sample. As this area had been completely covered with resist, it should have withstood ion implantation. Thus, the LSMO layer should have remained ferromagnetic. These measurements were performed in order to compare the magnetic response of the line pattern to an unpatterned sample.

Hysteresis curves at 300 K were obtained for the unpatterned control sample along the magnetocrystalline hard axes [100] and [010], as well as the magnetocrystalline easy axis [110]. Both hard axes were measured in order to be sure that the ferromagnetic signal on this part of the sample was not affected by the patterning of lines on the rest of the sample.

**Postprocessing data** The initial hysteresis curves at 50 K and 300 K were also used to compensate for the diamagnetic contribution from the STO substrate. The diamagnetic contribution is due to diamagnetism as well as Van Vleck paramagnetism [47]. As both diamagnetism and Van Vleck paramagnetism are known to be independent of temperature [13], the decision was made to simply average the diamagnetic contributions measured in both orientations at the two temperatures. This value was used as the slope for a first-degree polynomial that was subtracted from all data in order to remove the diamagnetic contribution of the substrate.

# Chapter 4

# Results and Discussion

*This chapter gives the results of the experimental work described in the previous chapter. First, the results of the process development are presented and discussed. The results of the patterning of thin film samples are then given, before the results of the magnetic characterization of thin film samples are given. Finally, the performance of the patterning process, as well as potential points of improvement, are discussed.*

## 4.1 SCIL Stamp Replication

The SCIL stamps were optically inspected after fully curing. The first SCIL stamp was found to have two small air bubbles embedded in the PDMS in one of the four quadrants. Apart from this, the stamp replication seemed to have worked well. The second stamp was found to be a near-perfect replica of the master wafer. No air bubbles or impurities were found during optical inspection.

Using a Hitachi S-5500 SEM, the nanoscale pattern of the first stamp was investigated. Figure 4.1 shows a micrograph of the line pattern in the top right quadrant of the stamp, with lines with 400 nm pitch.

The bright areas of the micrograph show the top surface of the line structure, while the dark areas show the bottom surface between the lines. The difference in signal intensity derives from the topographical contrast in secondary electron emission [48].

The bright areas in the micrograph appear wider than the dark areas. Measuring the relative width of the lines, the positive area fraction of the line pattern in the stamp seems to be approximately 61 %. This is partially due to the 5 nm layer of platinum-palladium alloy increasing the width of the lines by a total amount of 10 nm, but this layer does not explain the entire difference from the specified positive area fraction of 50 %. It is therefore likely that the line patterns in the master wafer are slightly narrower than specified, giving a positive area fraction of approximately 40 %, since the master wafer has the inverse pattern of the stamp. The periodicity of the pattern in the master wafer itself was not measured, due to its fragility.

The micrograph also shows some distortion near the edges of the field of view. This is likely due to charging effects associated with imaging of the stamp using a high-energy electron beam.

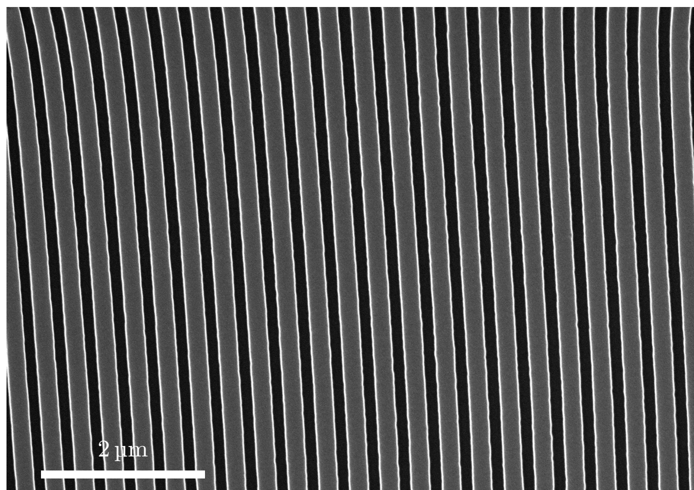


**Figure 4.1:** Scanning electron micrograph of SCIL stamp with 400 nm pitch line pattern. Acquired using a secondary electron (SE) detector with an acceleration voltage of $V_{\mathrm{acc}} = 20\,\mathrm{kV}$.

## 4.2 SCIL Adapter Development

### 4.2.1 Blind Hole Adapters

Using the single-sample and four-sample adapters provided by the workshop at the NTNU Department of Electronics and Telecommunications, several imprints were attempted. It became clear that the dimensions of the features of these machined parts were not precise enough to achieve good contact with the stamp during imprinting. It was also found that the holes for the samples were not able to sustain vacuum, leading to samples that did not separate from the stamp after imprinting. Using a tweezer, it was possible to pluck the samples from the SCIL stamp after unloading the stamp from the mask aligner. However, this put a lot of strain on the stamp pattern, reducing the stamp lifetime. In some cases, cured resist would be stuck in the stamp after manually removing the sample.

In order to get better contact with the vacuum surface of the wafer chuck, the reverse side of the polycarbonate adapter was covered with semiconductor dicing tape, with holes for the vacuum lines of the adapter. This improved the ability of the adapter to sustain vacuum, leading to imprints where the sample was released from the stamp during the separation step of the imprint process.

However, it was also found that the depth of the sample holes in the adapters was non-uniform, leading to samples that sat proud in some corners of the hole, while recessed in other places. Using a Veeco Dektak 150 profilometer on the single-sample adapter, the depth of the hole was found to exceed the height of the sample by 20 µm along one edge, and approximately 3 µm on the opposite edge. Similar results were found for the holes in the four-sample adapter. Since the SCIL technique is based on

conformal contact between the stamp and the sample, the geometry of these holes led to incomplete imprints, and in some cases, no imprint at all due to lack of contact between the stamp and the sample. In the ideal case, the sample should sit level with, or a few microns above, the surface of the adapter. Figure 4.2 shows several examples of incomplete imprints due to non-uniform holes in the adapters.

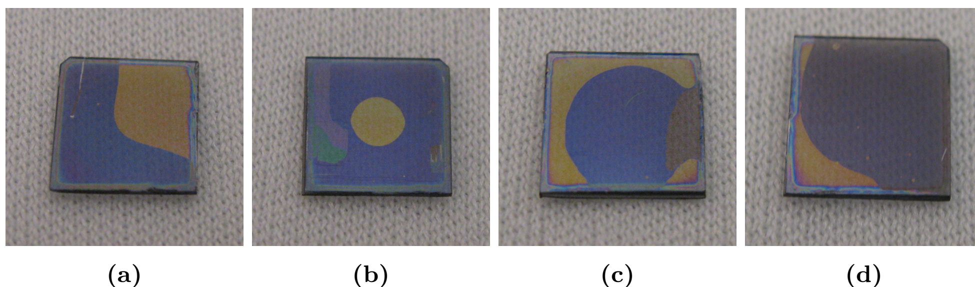

**(a)** **(b)** **(c)** **(d)**

**Figure 4.2:** Partial imprints. Blue area is successfully imprinted, while the yellow area is not patterned. **(a)** Top right corner not imprinted, due to too deep adapter in one corner. **(b)** Center not imprinted, due to too shallow adapter. Some resist stuck in stamp. **(c)** Edges not imprinted due to too deep adapter. Some resist stuck in stamp. **(d)** Left edge not imprinted, due to too deep adapter.

The adapter provided by the workshop at the NTNU Faculty of Natural Sciences and Technology was much closer to giving good imprints than the others, but was still somewhat too deep on one side of the milled hole. Figure 4.2d shows an imprint performed with this adapter.

Attempts were also made to use miscellaneous materials as padding underneath the sample, in order to raise it to the height of the adapter surface. It was found that most tapes, including dicing tape, Scotch tape, and Kapton tape, were too thick, leading to incomplete imprints as shown in Figure 4.2b due to the sample sitting too elevated in the adapter. Using a thin aluminium foil, with a thickness of 10 µm, a working spacer was created for one of the adapters.

### 4.2.2 Through Hole Adapters

Using the metal adapter, it was found difficult to ensure that the stainless steel plate was completely flat. The plate had some minor dents, which led to instabilities when placed on the wafer chuck. Another difficulty arose as the micrometer screws of the wafer chuck were found to not go below a height of approximately 150 µm. This meant that using a spacer was necessary for this type of adapter as well. However, due to the dents in the adapter, it was not used for imprints. Instead, the copper-coated FR-4 adapter was used.

The copper coated FR-4 adapter worked well. In order to protect the wafer chuck from scratches, the backside of the adapter was covered in semiconductor dicing tape. Height adjustment was performed using the three-point leveling mechanism of the wafer chuck. Complete imprints were achieved with no further problems.

## 4.3 SCIL Process Development

Several test samples were used to optimize the residual layer thickness after imprint and the residual layer etching time. All scanning electron micrographs presented in this section have been aquired with a SE detector using an acceleration voltage of 30 kV.

### 4.3.1 Residual Layer Thickness

Amonil MMS4 was spin coated at 4000, 5000, and 6000 rpm on different samples, and SCIL was performed on these samples. They were then manually cleaved, and the cross-section was inspected in a Hitachi S-5500 SEM. Figure 4.3 shows imprints performed with the 600 nm line pattern.

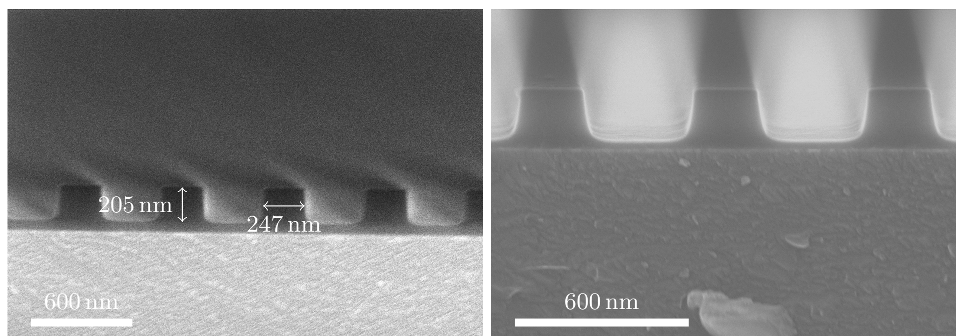


**(a)** Resist coated at 4000 rpm **(b)** Resist coated at 5000 rpm

**Figure 4.3:** Scanning electron micrographs of imprints using the line pattern with 600 nm pitch, showing decreasing residual layer thickness with increasing spin speed.

From the scanning electron micrographs, one can tell that the morphology of the imprinted lines closely matches the pattern specified by the manufacturer of the master wafer, as well as the pattern of the replicated SCIL stamp. The features were found to have a height of approximately 205 nm, as illustrated in Figure 4.3a. The pattern with 600 nm pitch was found to have a positive area fraction of approximately 40 %, leaving lines of resist with a width of 250 nm, with 350 nm separation. This correlates closely with the observations made upon inspection of the SCIL stamp. Similar positive area fractions were observed for imprint patterns with a different pitch.

The residual layer of the samples where Amonil MMS4 was spin coated at 4000 rpm was found to have a thickness of approximately 55 nm. Increasing the spin speed to 5000 rpm decreased the residual layer thickness to approximately 30 nm. At 6000 rpm, the residual layer was found to have a thickness of 20 nm. However, the slope of the sidewalls was found to deviate from vertical as the residual layer thickness was decreased. As near-straight sidewalls were wanted for the implantation mask, a spin speed of 5000 rpm was used for all following samples.

The residual layer thicknesses measured on the test samples do not completely fit with the resiudal layer formula as given in equation (3.1). The initial Amonil resist thickness after spin coating at 5000 rpm was measured to be approximately 150 nm by using a Hitachi S-5500 SEM to observe the crossection. By plugging the measured values for initial resist thickness, feature height and fraction of negative features into the equation, we get

$$R = T - H \cdot \frac{N}{P + N} \tag{4.1}$$

$$= 150\,\text{nm} - 205\,\text{nm} \cdot \frac{250}{600} = 64.6\,\text{nm} \tag{4.2}$$

This is thicker than the measured residual layer thickness of 30 nm.

The measurement of the initial resist thickness by SEM does not agree with measurements performed using a Filmetrics F20 reflectometer previously. By reflectometry, we found that the resist thickness of Amonil MMS4 when spin coated at 5000 rpm was approximately 180 nm [11]. The reflectometer calculates the thickness of the resist by observing laser light reflected from the air-resist and resist-sample interfaces. As such, it is sensitive to the refractive index and extinction coefficient of the materials. A likely explanation for the different results is that the reflectometer was poorly configured for measuring Amonil resist, giving erroneous measurement results for the initial resist thickness.

From these results, it seems likely that the physical process of resist flow when imprinting is more complex than what can be modelled by assuming that all resist removed from the positive areas of the stamp flow into the negative areas of the stamp. Some resist may flow outside the boundaries of the sample, reducing the overall thickness of the resist.

For further processes, 950K PMMA A2 was spin coated at 5000 rpm, before Amonil MMS4 was spin coated on top. The spin speed for the PMMA layer was chosen to be the same as the spin speed for the Amonil layer, as the thickness of the PMMA layer was not critical, and the process was simplified by having a single spin speed. Figure 4.4 shows a cross-section micrograph of a sample with PMMA and Amonil resists after imprinting.

### 4.3.2 Residual Layer Etch

Using the etching recipe described in Section 3.1.5, the optimal etching time for etching through the resist layer was found. Since the resist was to be used as a mask for subsequent ion implantation, it was deemed more important to preserve the height and sidewall profile of the structures than to guarantee complete etchthrough. Using test samples with Amonil lines with 600 nm pitch and no PMMA underlayer, the optimal etching time to etch through the residual layer was found to be 50 s. Given a residual layer thickness of 30 nm, this gives an etch rate of 36 nm/min. Figure 4.5 shows a scanning electron micrograph of a test sample with the 600 nm pitch line pattern after a residual layer etching time of 50 s.

Test samples with PMMA as well as Amonil were also etched. Samples with the 600 nm line pattern, as well as with the 400 nm line pattern, all required an etch time

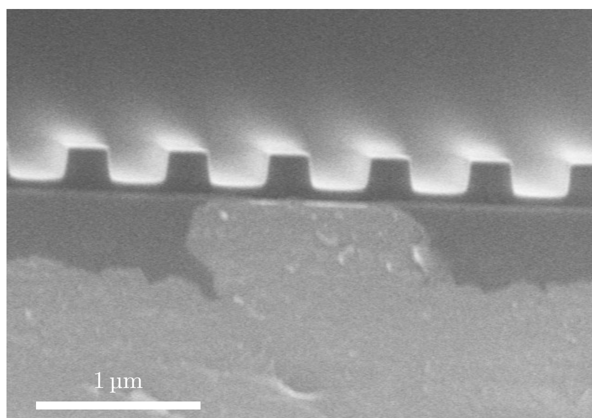


**Figure 4.4:** Scanning electron micrograph of cross-section of a test sample with 950K PMMA A2 and Amonil MMS4 resists after nanoimprinting.

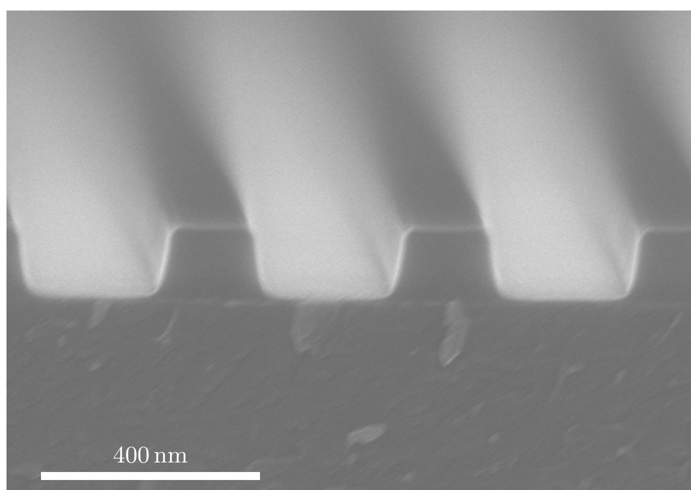


**Figure 4.5:** Scanning electron micrograph of test sample with a line pattern with 600 nm pitch after etching in $CF_4/CHF_3$ for 50 s, showing complete etchthrough of the residual layer.

of 110 s in order to etch through the residual layer of Amonil as well as the PMMA underlayer. Figure 4.6 shows cross-section micrographs of two such samples.

Optical endpoint detection was not used for the etch optimization, as detecting the optimal endpint from the reflected signal was found to be unreliable due to the topography of the resist pattern. Instead, the etch was run purely based on time. The etching time required to etch through the residual layer was found to be constant across several samples. The etch rate is highly dependent on the availability of etchant

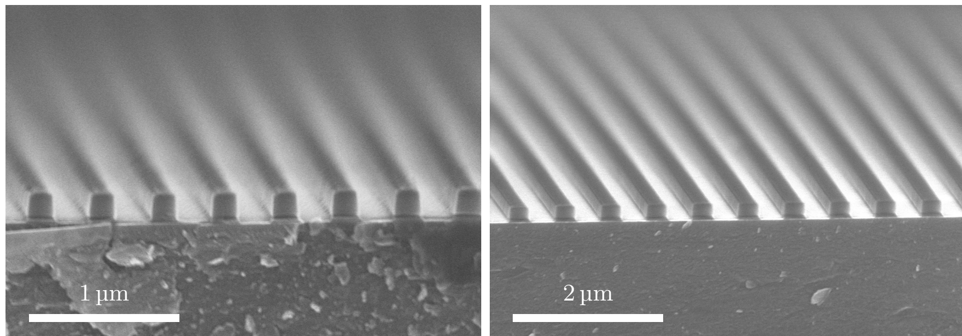


**(a)** 160 nm lines with 400 nm pitch **(b)** 250 nm lines with 600 nm pitch

**Figure 4.6:** Scanning electron micrographs of test samples after etching in $CF_4/CHF_3$ for 110 s, showing complete etchthrough of the Amonil residual layer and PMMA underlayer.

species and the pressure in the chamber. However, the etch recipe used for etching the residual layer uses gas flows and pressures that are well within the capabilities of the Plasmalab System 100, and the etching recipe was found to be very stable. We found that it was possible to run the etch recipe reproducibly with a reproducible etch rate.

The fact that the same etching time was found for the line pattern with 400 nm pitch as for the pattern with 600 nm pitch suggests that the aspect ratio is small enough for the etch rate to not differ much between the structures. Thus, an etch time of 110 s was used for all samples with PMMA A2 and Amonil MMS4 spin coated at 5000 rpm.

## 4.4 Thin Film Patterning

### 4.4.1 Thin Film Growth

A bilayer thin film of approximately 10 unit cells LFO on top of 90 unit cells LSMO was grown by PLD. The thin film was designated P50319. In situ monitoring by reflection high-energy electron diffraction (RHEED) indicated that the LSMO and LFO thin films were of good quality. The sample was characterized using a Veeco MultimodeV AFM. Figure 4.7 shows an atomic force micrograph of the sample microstructure after thin film growth, showing a step-and-terrace morphology. This structure is as expected, as it reflects the step-and-terrace structure of the intentionally miscut (001)-oriented Nb:STO substrate.

### 4.4.2 Substrate Conformal Imprint Lithography

SCIL was performed on sample P50319 using the 400 nm pitch area of the SCIL stamp and a polycarbonate adapter. The UV intensity at 320 nm was measured to be

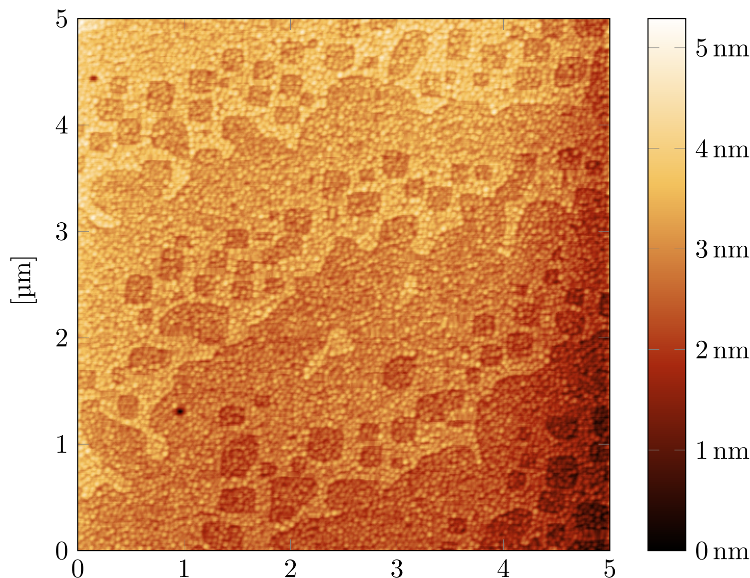


**Figure 4.7:** Atomic force micrograph of sample P50319 after thin film growth, showing step-and terrace morphology. *Courtesy of Fredrik K. Olsen.*

1.25 mW/cm$^2$, giving a total exposure time of 4000 s. Figure 4.8a shows a photograph taken of the sample after imprinting. From the photograph, one can easily see that the sample was only partially imprinted. However, this was deemed sufficient for a first sample to test the implantation and resist stripping steps, as the imprinted area exceeded $5 \times 5\,\text{mm}^2$, and the sample would need to be cut to $4 \times 4\,\text{mm}^2$ in order to fit on the VSM sample holder anyway.

The residual layer of Amonil and PMMA was then etched for 110 s according to the optimized etch recipe. After etching, the imprinted and non-imprinted areas had changed colors, as expected. The color of the resist is governed by its thickness, as light reflected from the air/resist and resist/substrate interfaces interfere constructively or destructively. Figure 4.8b shows a photograph of the sample after residual layer etching.

### 4.4.3 Ion Implantation and Mask Removal

After ion implantation, the resist mask was removed from the sample. It had been found that sonication for 5 min in acetone was sufficient to remove the resist from test samples that had not been implanted. However, for the implanted thin film sample, it was found that sonication in acetone was not sufficient. Figures 4.8c and 4.8d shows sample P50319 after 10 min and 30 min sonication in acetone. The images were taken using an optical microscope at 5x magnification.

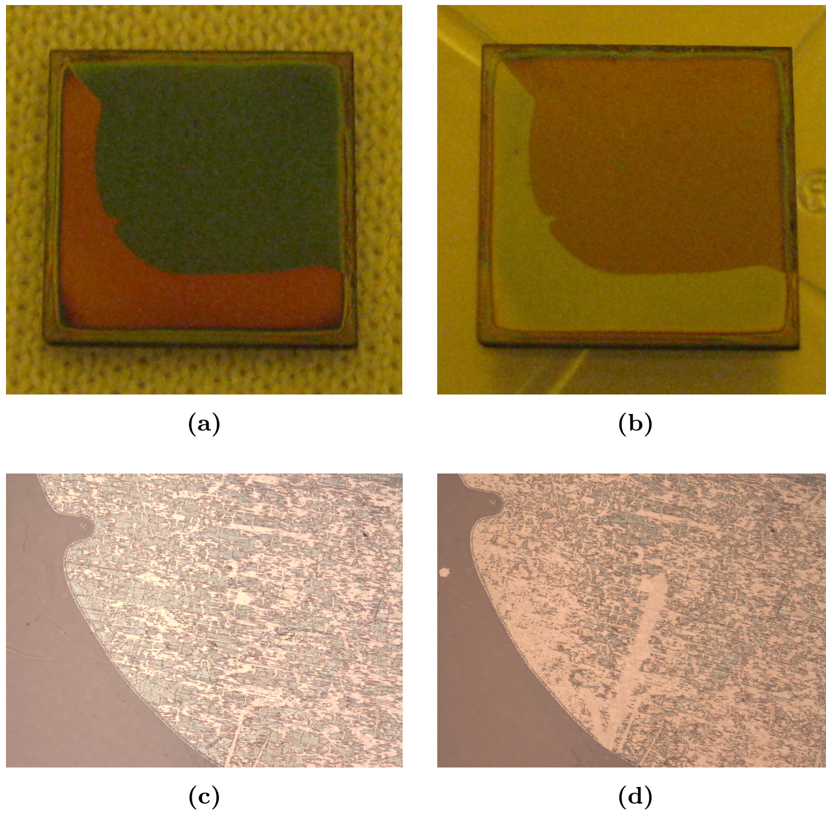

**Figure 4.8:** Sample P50319 at different stages during processing. **(a)** Sample after imprinting. **(b)** Sample after residual layer etch. **(c)** and **(d)** After attempted mask removal by sonication in acetone for 10 min and 30 min, respectively. Taken at 5 x magnification using an optical microscope.

In order to attempt to remove the rest of the resist, an acetone airbrush was used. By mixing acetone with pressurized nitrogen gas, the airbrush was able to remove most the residual resist through a combined physical and chemical method. Finally, the sample was rinsed in ethanol and blow-dried using nitrogen gas.

However, upon inspection using an AFM, it was clear that large areas of the sample still had a thin residual layer with a thickness of approximately 40 nm. In order to remove this layer, the sample was agitated for 60 s in glacial acetic acid, as acetic acid is known to remove PMMA [45]. Subsequent inspection revealed that the acetic acid was not able to remove the residual resist material. This suggests that the residual resist is not pure PMMA, but has had its properties modified by the $Ar^+$ implantation or Amonil resist.

### 4.4.4 Characterization

In order to ascertain whether the mask of Amonil and PMMA had held up to the ion implantation, the sample was characterized using an AFM. As shown in Figure 4.9, the sample showed a line pattern with a height of 8 nm, and a pitch of 400 nm.

The swelling of the implanted region is consistent with what has been observed by Folven *et al.* [6] for structures defined in thin films of LFO, using a chromium hard mask for ion implantation. A similar $Ar^+$ dose and energy was used for both processes. This indicates that the fabrication process developed in this work is able to produce embedded nanoscale magnetic structures by ion implantation of comparable quality to the structures patterned using EBL.

However, further inspection by AFM revealed several defects in the line pattern. In some places, a single line was missing, indicating that the resist structure had delaminated before implantation took place. In other places, the swelling of the thin film was measured to be smaller than 8 nm. This could mean that the region had not been implanted with the same dose as other parts, indicating that the resist had reflowed, covering the sample. It could also be an indication that the resist layer was not sufficiently thick to prevent ion implantation, leading to partially implanted regions underneath the resist lines. Figure 4.10 shows a $15 \times 15\,\mu\text{m}^2$ atomic force micrograph of an area of the sample. In the top right corner, residual resist is visible along some of the troughs of the pattern. In the bottom left corner, the feature height of the pattern is seen to be lower than in the center of the micrograph.

Measurements of the atomic force micrographs indicate that the lines of the implanted pattern have the same size as the lines imprinted in the resist. The width of the trenches was measured to be 160 nm, while the width of the peaks was measured to be 240 nm.

## 4.5 Magnetic Characterization of Thin Film Samples

*The VSM measures the total magnetic moment of the sample. Using the known dimensions of the ferromagnetic structures, as well as the thickness of the thin film, the magnetic moment per unit cell of LSMO, and consequently the magnetic moment per manganese atom, has been calculated. The diamagnetic contribution of the substrate, as found in Section 4.5.1, has also been subtracted from the reported measurements. The raw data for all post-processed figures presented in this section can be found in Appendix B.*

### 4.5.1 Diamagnetic Contribution

Hysteresis curves from −10 kOe to 10 kOe were acquired at temperatures $T = 50\,\text{K}$ and $T = 300\,\text{K}$ in the perpendicular as well as the parallel orientation for sample P50319, using a Quantum Design VersaLab with VSM module. Figure 4.11 shows the raw data for these hysteresis curves.

At high applied fields, when the LSMO thin film has been saturated, it is clear that a diamagnetic contribution from the substrate affects the measurements. A least

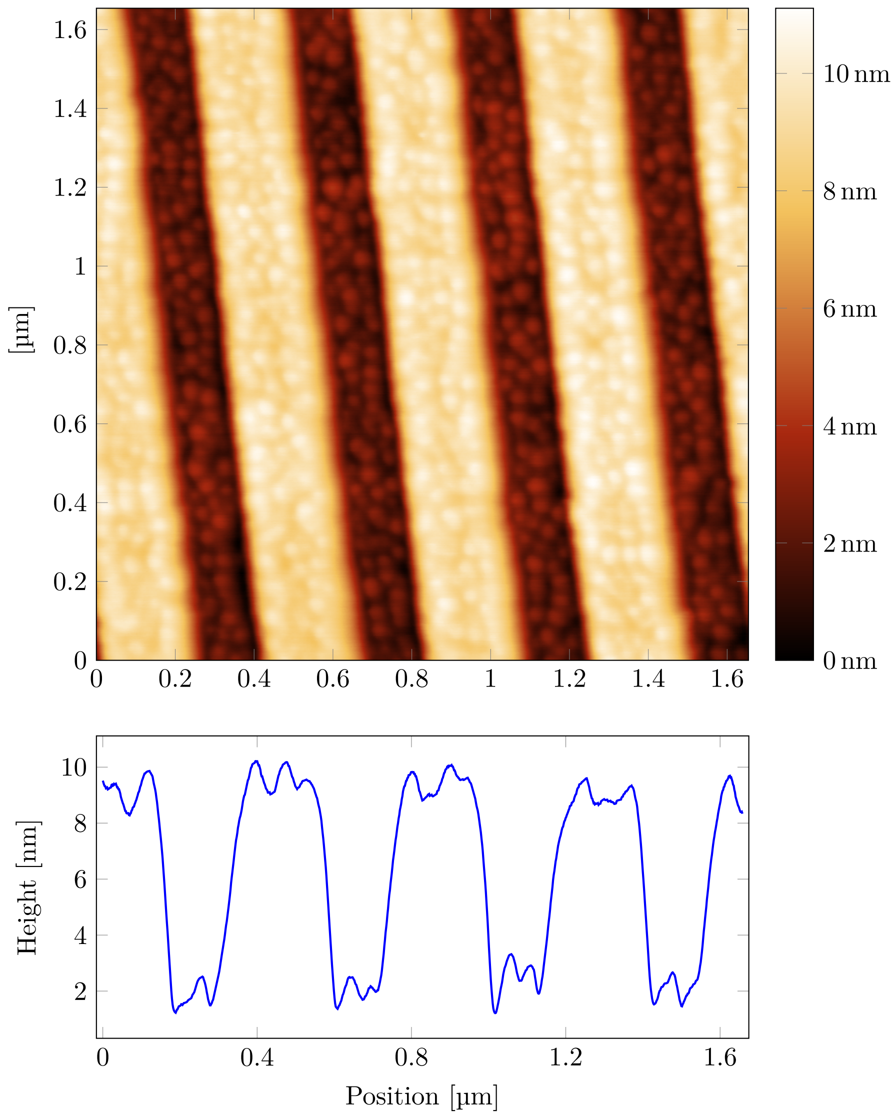


**Figure 4.9:** *Top*: Atomic force micrograph of sample P50319 after processing, showing a line pattern. Bright areas are approx. 8 nm higher than dark areas, due to swelling of the implanted regions of the thin film. *Bottom*: Line scan from atomic force micrograph of sample P50319 after processing, taken perpendicular to the line pattern.

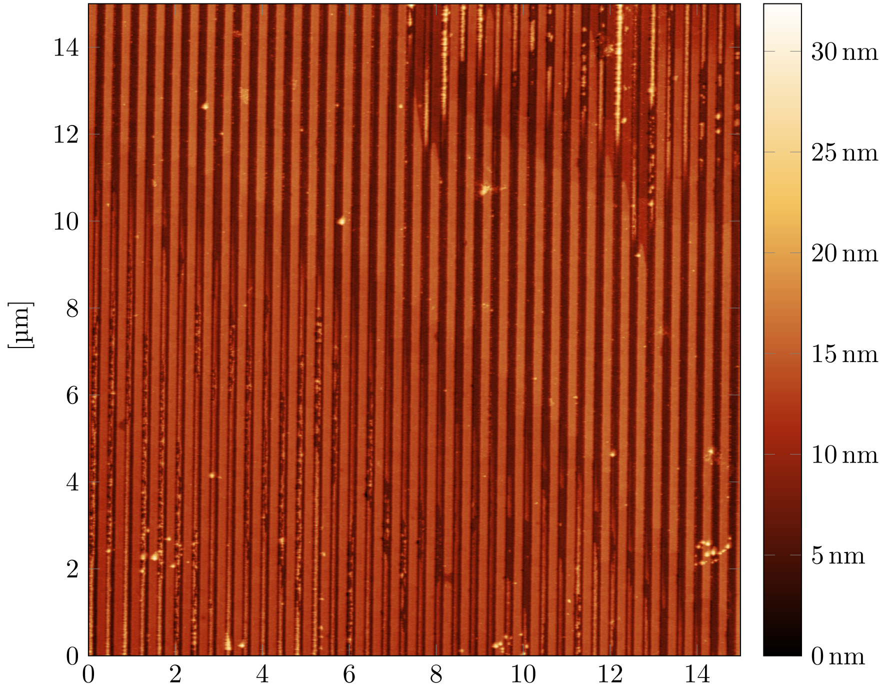


**Figure 4.10:** Atomic force micrograph of sample P50319 after processing, showing a line pattern. Bright areas are approx. 8 nm higher than dark areas, due to swelling of the implanted regions of the thin film. Residual resist is visible in parts of the micrograph.

squares linear regression was performed on the data between 7.5 kOe and 10 kOe, yielding a line with slope $-3.29 \cdot 10^{-9}$ emu/Oe at 50 K and $-3.98 \cdot 10^{-9}$ emu/Oe at 300 K in the perpendicular orientation, and $-3.40 \cdot 10^{-9}$ emu/Oe at 50 K and $-3.69 \cdot 10^{-9}$ emu/Oe at 300 K in the parallel orientation.

Averaging the slopes of the measurements at different temperatures and in different orientations, a value of $-3.59 \cdot 10^{-9}$ emu/Oe was found. Based on the volume of the substrate, the magnetic susceptibility was calculated to be $\chi_v = -5.61 \cdot 10^{-6}$. This is approximately one order of magnitude larger than what has been reported in literature for pure STO [47], but fits well with results for 0.05 wt% Nb:STO [19].

### 4.5.2 Saturation Magnetic Moment

The saturation magnetic moment of sample P50319 was measured as a function of temperature using a Quantum Design VersaLab with VSM module. Figure 4.12 shows the saturation magnetic moment as a function of temperature for the two orientations.

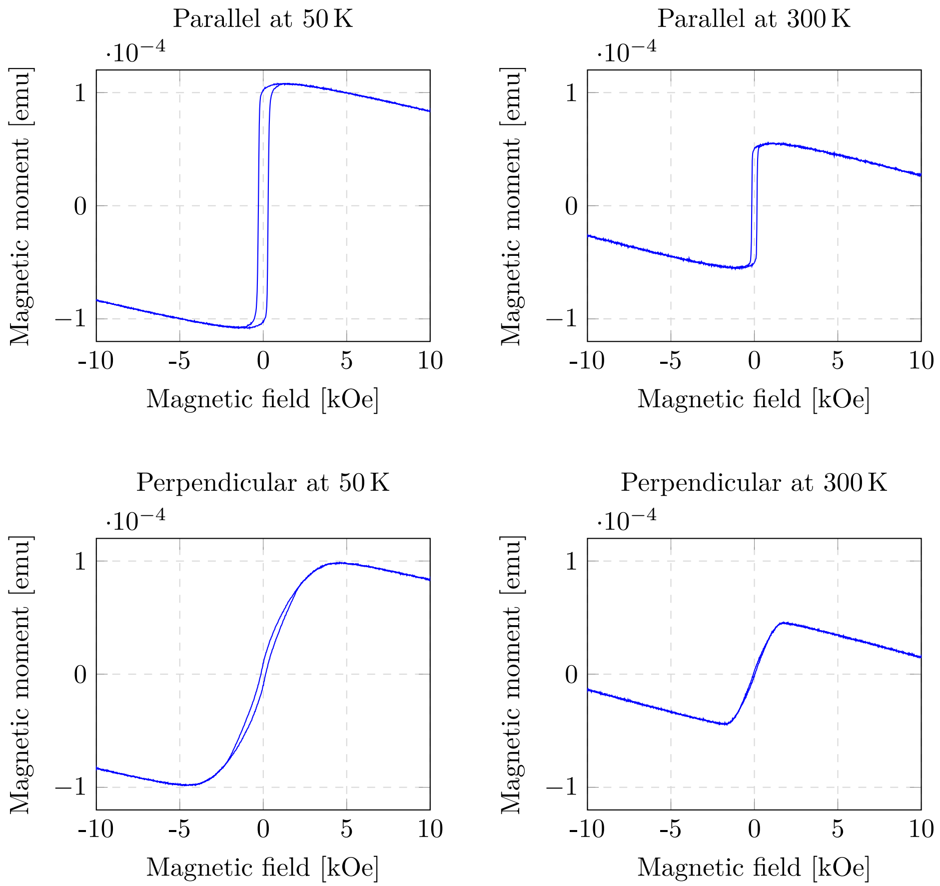


**Figure 4.11:** Hysteresis curves parallel with and perpendicular to the line pattern at 50 K and 300 K, showing a diamagnetic contribution at high applied field.

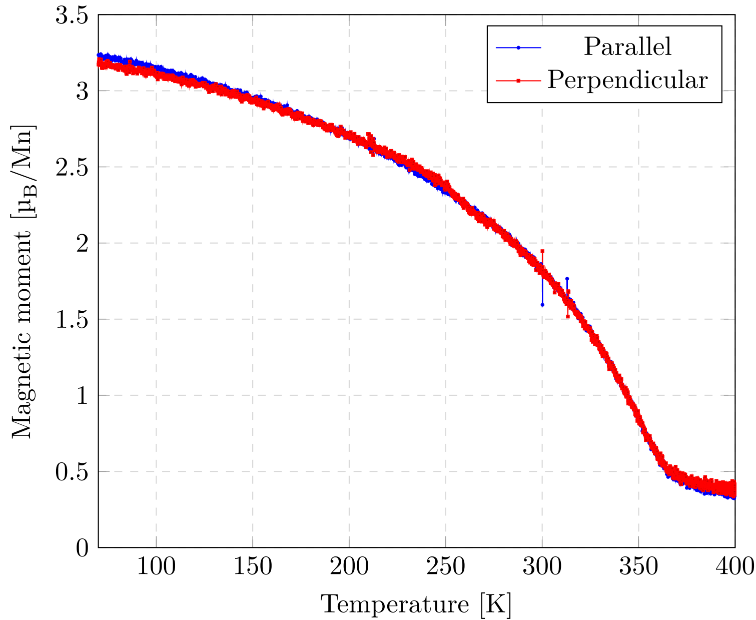


**Figure 4.12:** Saturation magnetic moment versus temperature for two orientations of sample P50319.

From the figure, we observe that the saturation magnetization decreases with temperature, as is expected when the thermal noise of the system increases, preventing all spins from being perfectly aligned. The Curie temperature can be defined in several different ways, including the inflection point or the point of largest curvature of the convex part of the magnetization vs. temperature curve, or the intersection points between two tangent lines drawn from below and above the point of largest curvature [49, 50]. In this work, the point of largest curvature on the magnetization vs. temperature curve has been used. Using a Savitzky-Golay filter [51], fitting successive sets of 101 data points to a third degree polynomial, the measurement data can be smoothened, such that it can be numerically differentiated, and the point of largest curvature found. The Curie temperature was found to be 363.6 K in the parallel orientation, and 364.4 K in the perpendicular orientation. The small difference between the two orientations is clearly due to imperfections in measurement and data processing, in particular the filtering of the data.

A Curie point of approximately 364 K fits well with what has been reported in literature for thin films of $La_{0.7}Sr_{0.3}MnO_3$, where Curie temperatures up to 370 K have been reported [22]. This suggests that the LSMO thin film does not have many oxygen vacancies, as the presence of oxygen vacancies would lower the Curie temperature dramatically [52].

However, the saturation magnetic moment of the thin film at 70 K of approximately

3.2 $\mu_B$ is smaller than the theoretical saturation magnetic moment of 3.7 $\mu_B$. The degree of magnetization may increase as the temperature is lowered to 0 K, but this is apparently not enough to account for the low measured saturation magnetic moment. The calculation of the magnetic moment per manganese atom was performed assuming that all $N = 90$ unit cells of the LSMO thin film are ferromagnetic. However, it is well known that a magnetic dead layer with a thickness of a few unit cells forms at the LSMO/STO interface. This suggests that using a film thickness of $N \approx 86$ unit cells could give a more accurate value for the magnetic moment per atom. This would, however, not be sufficient to explain the small magnetic moment.

It is therefore likely that there are parts of the sample that are nonmagnetic. The magnetic moment per magnanese atom has been calculated by assuming that the entire sample consists of 160 nm wide ferromagnetic lines with 400 nm pitch, and has a thickness of 90 unit cells. There are several factors that may explain the lower than expected magnetic moment. Firstly, the argon ion implantation may disrupt the LSMO lattice past the edge of the swollen area, by straining the crystal structure, leading to ferromagnetic lines that are narrower than what the physical structure suggests. Secondly, ferromagnetic lines may be missing, due to damage to the resist mask before ion implantation. Thirdly, the argon ion implantation may have partially penetrated the mask, passivating parts of the thin film close to the surface. These are questions that require further exploration.

The magnetic moment vs temperature curve does not proceed to zero magnetic moment at high temperature, but flattens out at a residual moment of approximately 0.4 $\mu_B$/Mn. Above the Curie temperature, the LSMO thin film becomes paramagnetic. Since the magnetization curves were obtained in an applied magnetic field of 5 kOe, this residual magnetization may be due to the paramagnetic response of the LSMO thin film above the Curie temperature. The regions of the thin film that were implanted with $Ar^+$ ions, and thus no longer were ferromagnetic, may also contribute with a paramagnetic signal, as the manganese atoms in this region still have unpaired electrons that may align with the applied field. However, this contribution would also exist below the Curie temperature of the undamaged part of the sample, and therefore have been removed together with the diamagnetic contribution of the substrate. The LFO film should not contribute to the observed magnetic moment, as the temperature is well below its Néel temperature of 740 K [29].

However, it is also possible that this magnetic moment originates from the substrate. It has been shown that niobium-doped STO may become ferromagnetic at sufficient doping concentrations of niobium. Liu *et al.* [19] have shown ferromagnetic behavior in 0.5 wt% Nb:STO. However, they did not find a ferromagnetic signal in 0.05 wt% Nb:STO, as was used in this project.

A hysteresis measurement was performed parallel with the line pattern at 400 K in order to investigate the origin of the magnetic moment above the Curie temperature of the LSMO thin film. The magnetic field was sweeped to ± 10 kOe. Figure 4.13 shows the hysteresis curve.

A ferromagnetic response with a coercive field of approximately 80 Oe is clearly visible in the hysteresis curve. This shows presence of ferromagnetism above the Curie temperature, which means that the magnetic moment visible above $T_c$ in Figure 4.12

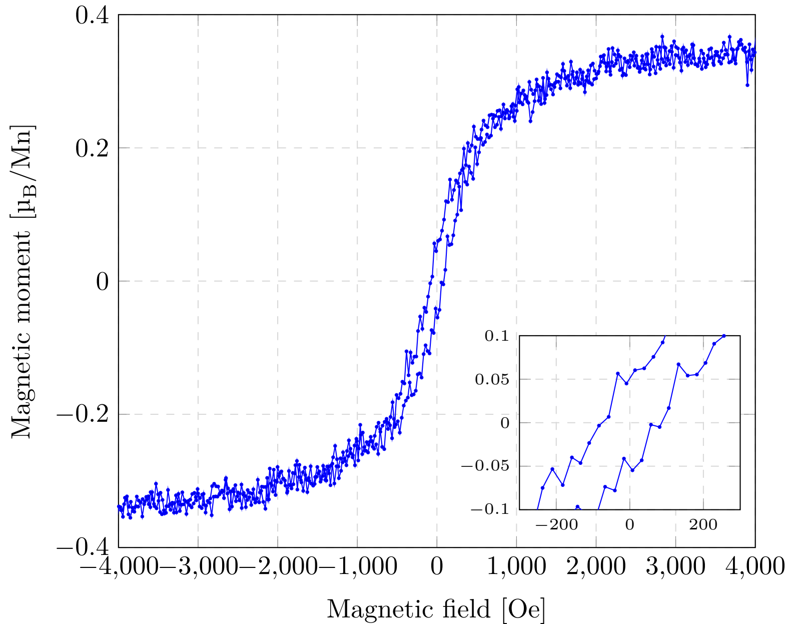


**Figure 4.13:** Hysteresis parallel with the line pattern at 400 K, which is above $T_c$ for LSMO. Inset: Detailed view of the hysteresis curve around the origin.

cannot be fully explained by a paramagnetic response of LSMO. This measurement suggests that the signal originates from the Nb:STO substrate, the sample holder, or contamination in the VSM chamber. Similar magnetic response above $T_c$ has also been observed for (111)-oriented LSMO thin films grown on Nb:STO, as well as in bare Nb:STO substrates by other users of the instrument [53]. Investigation into the origin of the signal is ongoing, and considered out of the scope of this work.

### 4.5.3 Magnetic Hysteresis

Magnetic hysteresis curves were obtained by measuring the magnetic moment of sample P50319 as a function of applied magnetic field in a Quantum Design VersaLab with VSM module.

#### Unpatterned Control Sample

Figure 4.14 shows hysteresis curves for three different crystal directions of the unpatterned control sample at 300 K, with an applied magnetic field of $H = \pm 500$ Oe.

From this figure, it is clear that the control sample is ferromagnetic, and that there is little difference between the magnetocrystalline easy and hard axes. From the data, the coercive field was measured to be 4.4 Oe along the [100] hard axis, 4.7 Oe along

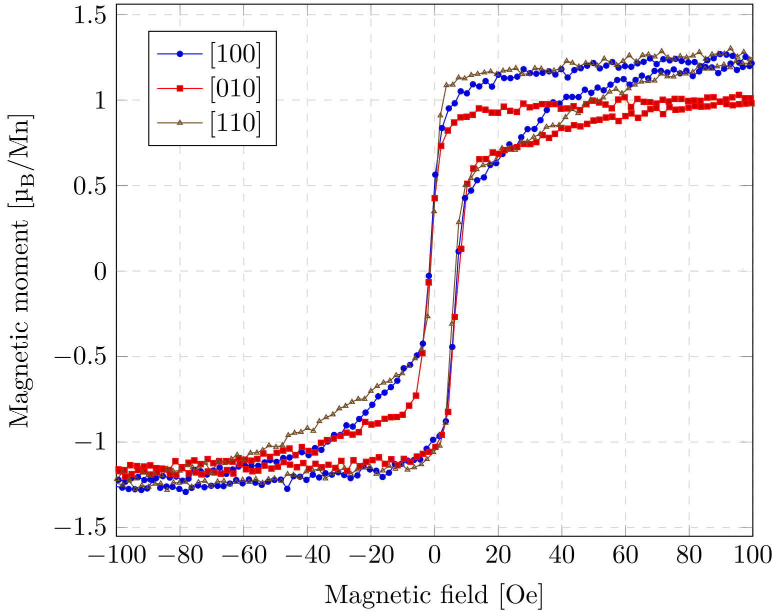


**Figure 4.14:** Hysteresis curve for the unpatterned control sample along several crystal axes at 300 K, with a maximum applied field of ± 500 Oe.

the [010] hard axis, and 3.9 Oe along the [110] easy axis. These values for the coercive field are of the same order of magnitude as has been reported for single-layer LSMO thin films of comparable thickness [26, 54].

The measurements also show little difference between the hysteresis behavior in the [100] and [010] directions of the sample. This confirms that this part of the sample was indeed not patterned, and that any anisotropy seen between the [100] direction parallel to the line pattern and [010] direction perpendicular to the line pattern of the patterned part of the sample derives from the patterning.

#### 400 nm Line Pattern

The magnetic moment in the part of the sample with a 400 nm line pattern was measured in the [100] direction parallel to the lines, and in the [010] direction perpendicular to the lines.

Figure 4.15 shows hysteresis curves obtained when applying a magnetic field parallel to the nanoscale line pattern. Using helium cooling, hysteresis curves were obtained at temperatures from 50 K to 350 K in 25 K intervals by sweeping the applied magnetic field between −1200 Oe and 1200 Oe.

One can clearly see that the hysteresis curve takes on a different shape compared to the hysteresis curve of the unpatterned part of the sample. The coercive field at

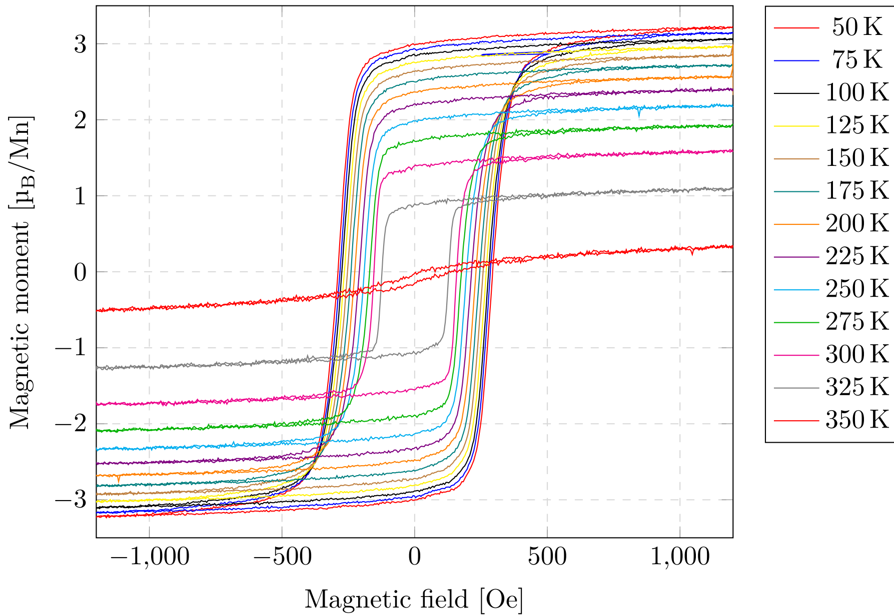


**Figure 4.15:** Hysteresis curves at 25 K intervals from 50 K to 350 K of sample P50319 with field applied parallel to the nanoscale line pattern. The magnetic field was swept from 1200 Oe to −1200 Oe and back.

300 K increases from approximately 4 Oe for the unpatterned control sample to more than 150 Oe parallel to the line pattern. The saturation magnetic moment is observed to decrease with decreasing temperature, as expected from Bloch's law [12].

Figure 4.16 shows hysteresis curves obtained when applying a magnetic field perpendicular to the nanoscale line pattern. Using helium cooling, hysteresis curves were obtained at temperatures from 50 K to 350 K in 25 K intervals by sweeping the applied magnetic field between −5 kOe and 5 kOe.

From the figure, it is clear that the hysteresis behavior when applying a field perpendicular to the line pattern is different from when applying the field parallel to the line pattern. The coercive field at 300 K is reduced to approximately 80 Oe, and a higher applied field is required to reach magnetic saturation. The saturation magnetic moment is observed to be similar to the case where the magnetic field was applied parallel to the line pattern, as expected.

From the hysteresis curves, it is clear that the magnetic response to a field applied parallel to the lines is consistent with that of a shape-induced magnetic easy axis, while the magnetic response to a field applied perpendicular to the lines is consistent with that of a magnetic hard axis. This suggests that there is a strong shape-induced magnetic anisotropy in these structures, as would be expected for near-infinitely long, narrow structures. This suggests that there is strong correlation between the swelling

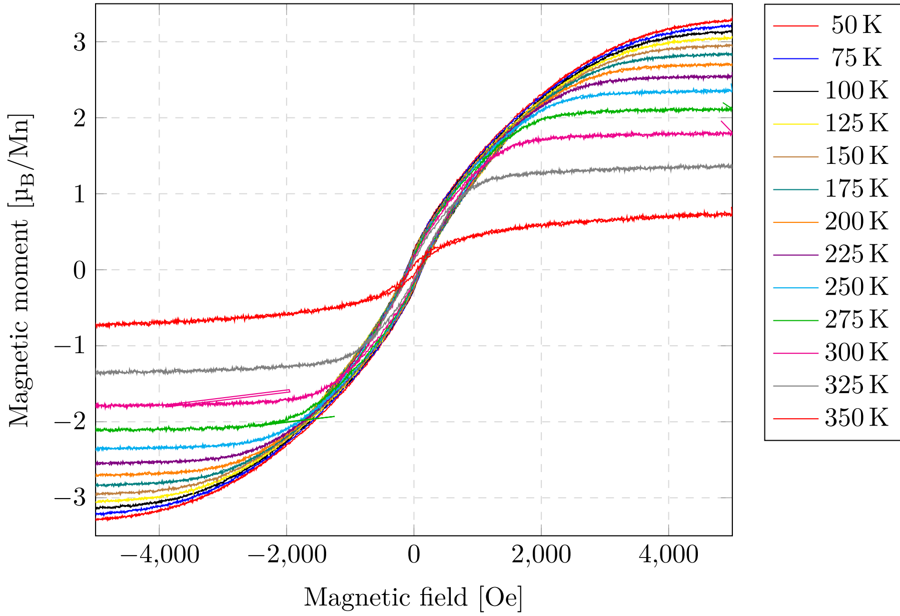


**Figure 4.16:** Hysteresis curves at 25 K intervals from 50 K to 350 K of sample P50319 with field applied perpendicular to the nanoscale line pattern. The applied magnetic field was swept from 5 kOe to −5 kOe and back.

of the implanted areas of the sample as seen by AFM, and the shape of the ferromagnetic structures in the sample.

**Coercive Field and Remanent Magnetization** Analyzing the data from hysteresis curves obtained parallel to and perpendicular to the line pattern, the coercive field and remanent magnetization was obtained. Both values were extracted by linear interpolation between data points, yielding the field and magnetization values at the axis intercepts. As the hysteresis loops weren't necessarily perfectly symmetric around the origin, the coercive field was defined as the half width of the hysteresis loop, measured as the difference between the positive and negative coercive fields divided by two:

$$H_c = \frac{H_{c,\mathrm{pos}} - H_{c,\mathrm{neg}}}{2} \tag{4.3}$$

The remanent magnetization was defined in the same way, measured as the difference between the positive and negative remanent magnetization divided by two:

$$M_r = \frac{M_{r,\mathrm{pos}} - M_{r,\mathrm{neg}}}{2} \tag{4.4}$$

Figure 4.17 shows the coercive field of sample P50319 as a function of temperature for both sample orientations with respect to the applied magnetic field.

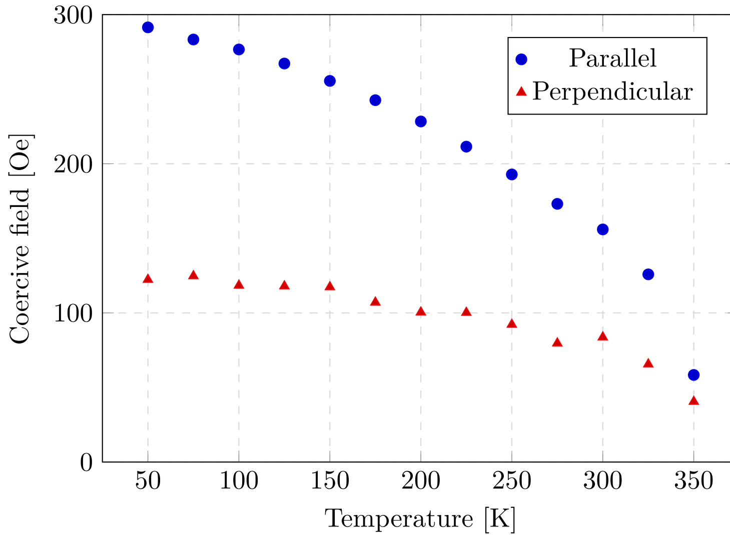


**Figure 4.17:** Coercive field of sample P50319 parallel to and perpendicular to the line pattern

The coercive field is seen to be higher for both sample orientations compared to the unpatterned control sample. This is as expected from theory, as the narrow structures are expected to take on a single-domain configuration due to the strong shape anisotropy. Thus, there are no domains that can grow when a field is applied, and the only mechanism for alignment of the spins of the material with the applied field is by rotation of the magnetization of the entire structure.

Figure 4.18 shows the remanent magnetization of sample P50319 as a function of temperature for both sample orientations with respect to the applied magnetic field.

From the remanence curve, it is clear that the remanent magnetization is much higher after applying a magnetic field parallel to the lines, compared to perpendicular to the lines. This fits well with the general shape of the hysteresis curves, as seen above. This further supports the conclusion that the patterning of magnetic lines has worked, as magnetic anisotropy is clearly visible.

## 4.6 Further Process Development

The magnetic measurement results, as presented in Section 4.5, show that the patterning process as developed in this work is able to produce highly anisotropic nanoscale magnetic structures over extended areas. While some residue from the ion implantation mask was found to remain on the surface of the sample, this did not affect the magnetic measurements by VSM, as it is not a surface sensitive technique.

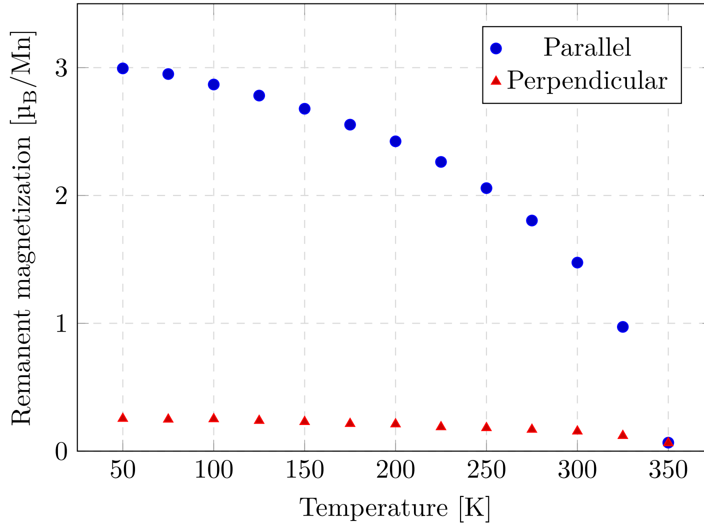


**Figure 4.18:** Remanent magnetization of sample P50319 after applying a magnetic field parallel to and perpendicular to the line pattern

However, if the patterning process is to be used as part of a larger multi-step manufacturing process, or if surface-sensitive techniques such as x-ray magnetic dichroism photoemission electron microscopy (XMCD/XMLD-PEEM) or magnetic force microscopy (MFM) are to be used to investicate the microscopic domain structure of the patterned samples, the patterning process should be modified to allow for reliable removal of the resist mask after ion implantation.

Since PMMA readily dissolves in acetone, and lift-off of the Amonil layer by dissolution of the PMMA layer has been shown to work on patterned samples before ion implantation, one possible approach would be to increase the thickness of the PMMA underlayer in order to ensure that the layer was thick enough for lift-off to work. In this work, 950K PMMA A2 with a thickness of approximately 50 nm was used. If the PMMA thickness was increased to 80 nm or higher, a thicker implantation mask could be made. However, since the selectivity of the residual layer etch between Amonil and PMMA was found to be approximately 1:1 in this work, a different etch recipe with higher selectivity would be required to transfer the imprinted pattern from the Amonil resist to the PMMA resist.

Another possibility would be to replace the PMMA underlayer with a metal underlayer, such as chromium. A chromium underlayer could easily be removed in an acetic acid wet etch after ion implantation [6]. One could either use a thin chromium layer covering the entire sample, allowing $Ar^+$ ions to pass through it during ion implantation, or a thick chromium layer. If a thick layer was used, it would need to be etched using the Amonil resist as a mask. Possible patterning methods include chlorine-based ICP-RIE, or ion beam etching.

# Chapter 5

# Conclusion and Outlook

A novel patterning method for creating embedded magnetic nanostructures in complex oxide thin films was demonstrated in this work. Using substrate conformal imprint lithography, with a custom adapter to allow for square samples, the nanoscale line pattern of a master wafer was successfully transferred to a resist layer. This resist layer was then successfully used as a mask for ion implantation of $Ar^+$, disrupting the magnetic order of the unprotected areas of a complex oxide thin film.

Characterization by vibrating sample magnetometer shows that the patterned sample exhibits large shape anisotropy, as expected from magnetic structures with finite width and height, and near-infinite length. The nanoscale pattern in the thin film shows a saturation magnetic moment of $3.2\,\mu_B$/Mn, which is somewhat lower than the bulk value of $3.7\,\mu_B$/Mn. The coercive field of the structures was found to increase by more than an order of magnitude compared to unpatterned thin films. A coercivity of 290 Oe was measured parallel to the nanoscale line pattern at 50 K, while a coercivity of 125 Oe was measured perpendicular to the line pattern.

It was shown that it is possible to perform substrate conformal imprint lithography on small samples that do not fit in the wafer chuck designed for 2 inch wafers by using a simple adapter machined from a copper-coated circuit board. By utilizing the sample leveling mechanism of the wafer chuck, the conformal contact necessary for imprinting to work was achieved reliably and reproducibly.

This work has also shown that it is possible to use a dual-layer mask of Amonil and PMMA resists with a total thickness of approximately 180 nm as an implantation mask for ion implantation of 50 keV $Ar^+$ ions. However, more work is required in order to be able to reliably remove the resist mask after ion implantation. Several suggestions for how to improve the mask removal step of the process have been presented.

## 5.1 Outlook

The process developed in this work makes it possible to further investigate the spin-flop coupling in nanostructured bilayers of LFO and LSMO, and how it affects the magnetostatic properties of the LSMO layer. A transition between parallel (colinear) and perpendicular (spin-flop) alignment of magnetization between the layers has pre-

viously been investigated by Folven *et al.* [8]. Using x-ray magnetic dichroism with PEEM, they found that colinear alignment dominated in 200 nm wide lines, while spin-flop alignment dominated in 500 nm wide lines. Using the patterning technique presented in this work, it would be possible to further investigate this phenomenon, to find whether the change from spin-flop to colinear alignment affects the hysteretic behavior of the LSMO layer, and further understand the effect of the exchange coupling between LFO and LSMO thin film layers.

# Bibliography


1. APS. *This Month in Physics History - November 17 - December 23, 1947: Invention of the First Transistor* 2000.
2. Baibich, M., Broto, J., Fert, A., *et al.* Giant Magnetoresistance of (001)Fe/(001)Cr Magnetic Superlattices. *Physical Review Letters* **61,** 2472–2475 (1988).
3. Wolf, S. A., Awschalom, D. D., Buhrman, R. A., *et al.* Spintronics: A Spin-Based Electronics Vision for the Future. en. *Science* **294,** 1488–1495 (2001).
4. Ramirez, A. P. Colossal magnetoresistance. *Journal of Physics: Condensed Matter* **9,** 8171 (1997).
5. Takamura, Y., Chopdekar, R. V., Scholl, A., *et al.* Tuning Magnetic Domain Structure in Nanoscale $La_{0.7}Sr_{0.3}MnO_3$ Islands. *Nano Letters* **6,** 1287–1291 (2006).
6. Folven, E., Tybell, T., Scholl, A., *et al.* Antiferromagnetic Domain Reconfiguration in Embedded $LaFeO_3$ Thin Film Nanostructures. *Nano Letters* **10,** 4578–4583 (2010).
7. Folven, E., Scholl, A., Young, A., *et al.* Effects of nanostructuring and substrate symmetry on antiferromagnetic domain structure in $LaFeO_3$ thin films. *Physical Review B* **84,** 220410 (2011).
8. Folven, E., Scholl, A., Young, A., *et al.* Crossover from Spin-Flop Coupling to Collinear Spin Alignment in Antiferromagnetic/Ferromagnetic Nanostructures. *Nano Letters* **12,** 2386–2390 (2012).
9. Folven, E., Takamura, Y. & Grepstad, J. K. X-PEEM study of antiferromagnetic domain patterns in $LaFeO_3$ thin films and embedded nanostructures. *Photoelectron microscopy, Time resolved pump-probe PES* **185,** 381–388 (2012).
10. Takamura, Y., Folven, E., Shu, J. B., *et al.* Spin-Flop Coupling and Exchange Bias in Embedded Complex Oxide Micromagnets. *Physical Review Letters* **111,** 107201 (2013).
11. Mellbye, A. *Nanopatterning of Magnetic Oxide Thin Films* Master's Project (NTNU, Trondheim, 2014).
12. O'Handley, R. C. *Modern Magnetic Materials: Principles and Applications* en. ISBN: 9780471155669 (Wiley, 1999).
13. Kittel, C. *Introduction to Solid State Physics* en. ISBN: 9780471415268 (Wiley, 2004).

14. Zener, C. Interaction Between the d Shells in the Transition Metals. *Physical Review* **81,** 440–444 (1951).

15. Zener, C. Interaction between the d-Shells in the Transition Metals. II. Ferromagnetic Compounds of Manganese with Perovskite Structure. *Physical Review* **82,** 403–405 (1951).

16. Campos, M. F. d., Landgraf, F. J. G., Saito, N. H., *et al.* Chemical composition and coercivity of $SmCo_5$ magnets. *Journal of Applied Physics* **84,** 368–373 (1998).

17. Monsen, Å. *On the properties of* $La_{0.7}Sr_{0.3}MnO_3$ *thin films on (001)* $SrTiO_3$ *substrates* en. PhD thesis (NTNU, Trondheim, 2012).

18. Marques, A. C. L. S. Advanced Si pad detector development and $SrTiO_3$ studies by emission channeling and hyperfine interaction experiments. eng (2009).

19. Liu, Z. Q., Lü, W. M., Lim, S. L., *et al.* Reversible room-temperature ferromagnetism in Nb-doped $SrTiO_3$ single crystals. *Physical Review B* **87,** 220405 (2013).

20. Jin, S., Tiefel, T. H., McCormack, M., *et al.* Thickness dependence of magnetoresistance in La-Ca-Mn-O epitaxial films. *Applied Physics Letters* **67,** 557–559 (1995).

21. Dagotto, E., Hotta, T. & Moreo, A. Colossal magnetoresistant materials: the key role of phase separation. *Physics Reports* **344,** 1–153 (2001).

22. Urushibara, A., Moritomo, Y., Arima, T., *et al.* Insulator-metal transition and giant magnetoresistance in $La_{1-x}Sr_xMnO_3$. *Physical Review B* **51,** 14103–14109 (1995).

23. O'Brien, M. C. M. & Chancey, C. C. The Jahn-Teller effect: An introduction and current review. *American Journal of Physics* **61,** 688–697 (1993).

24. Konoto, M., Kohashi, T., Koike, K., *et al.* Magnetic domain structure of a $La_{0.7}Sr_{0.3}MnO_3$ (001) surface observed by a spin-polarized scanning electron microscope. *Applied Physics Letters* **84,** 2361–2363 (2004).

25. Cesaria, M., Caricato, A. P., Maruccio, G., *et al.* LSMO - growing opportunities by PLD and applications in spintronics. en. *Journal of Physics: Conference Series* **292,** 012003 (2011).

26. Monsen, Å., Boschker, J. E., Macià, F., *et al.* Thickness dependence of dynamic and static magnetic properties of pulsed laser deposited $La_{0.7}Sr_{0.3}MnO_3$ films on $SrTiO_3$(001). *Journal of Magnetism and Magnetic Materials* **369,** 197–204 (2014).

27. Monsen, Å. F., Song, F., Li, Z. S., *et al.* Surface stoichiometry of $La_{0.7}Sr_{0.3}MnO_3$ during in vacuo preparation; A synchrotron photoemission study. *Surface Science* **606,** 1360–1366 (2012).

28. Kim, B., Kwon, D., Song, J. H., *et al.* Finite size effect and phase diagram of ultra-thin $La_{0.7}Sr_{0.3}MnO_3$. *Solid State Communications* **150,** 598–601 (2010).

29. Seo, J. W., Fullerton, E. E., Nolting, F., *et al.* Antiferromagnetic $LaFeO_3$ thin films and their effect on exchange bias. en. *Journal of Physics: Condensed Matter* **20,** 264014 (2008).
30. Schulthess, T. C. & Butler, W. H. Consequences of Spin-Flop Coupling in Exchange Biased Films. *Physical Review Letters* **81,** 4516–4519 (1998).
31. Koon, N. C. Calculations of Exchange Bias in Thin Films with Ferromagnetic/ Antiferromagnetic Interfaces. *Physical Review Letters* **78,** 4865–4868 (1997).
32. Cui, Z. *Nanofabrication: Principles, Capabilities and Limits* en. ISBN: 978-0-387-75576-2 (Springer, 2008).
33. Delamarche, E., Schmid, H., Michel, B., *et al.* Stability of molded polydimethylsiloxane microstructures. en. *Advanced Materials* **9,** 741–746 (1997).
34. Ji, R., Hornung, M., Verschuuren, M. A., *et al.* UV enhanced substrate conformal imprint lithography (UV-SCIL) technique for photonic crystals patterning in LED manufacturing. *Microelectronic Engineering. The 35th International Conference on Micro- and Nano-Engineering (MNE)* **87,** 963–967 (2010).
35. Verschuuren, M. A. *Substrate Conformal Imprint Lithography for Nanophotonics* PhD thesis (Utrecht University, Utrecht, 2010).
36. SUSS. *(Nano) Imprint Solutions On Suss Mask Aligners*
37. Liu, C. *Foundations of MEMS* 2nd ed. ISBN: 9780273752240 (Pearson Education, 2012).
38. Bass, J. D. *Elasticity of Minerals, Glasses, and Melts* en. in *Mineral Physics & Crystallography: A Handbook of Physical Constants* (ed Ahrens, T. J.) (American Geophysical Union, 1995), 45–63. ISBN: 9781118668191.
39. Callister, W. D. & Rethwisch, D. G. *Materials Science and Engineering* 8th edition. ISBN: 9780470505861 (John Wiley & Sons, 2011).
40. Quirk, M. & Serda, J. *Semiconductor Manufacturing Technology* ISBN: 9780130815200 (Prentice Hall, 2001).
41. Welch, C. *Nanoscale Etching in Incuctively Coupled Plasmas* tech. rep. (Oxford Instruments Plasma Technology, 2011).
42. AMO. *AMONIL & AMOPRIME - low viscosity imprint resist and adhesion promoter*
43. Barbillon, G., Hamouda, F., Held, S., *et al.* Gold nanoparticles by soft UV nanoimprint lithography coupled to a lift-off process for plasmonic sensing of antibodies. *Microelectronic Engineering. The 35th International Conference on Micro- and Nano-Engineering (MNE)* **87,** 1001–1004 (2010).
44. MicroChem. *NANO PMMA and Copolymer*
45. Chavez, K. L. & Hess, D. W. Removal of Resist Materials Using Acetic Acid. en. *Journal of The Electrochemical Society* **150,** G284–G291 (2003).
46. Foner, S. Versatile and Sensitive Vibrating-Sample Magnetometer. *Review of Scientific Instruments* **30,** 548–557 (1959).

47. Frederikse, H. P. R. & Candela, G. A. Magnetic Susceptibility of Insulating and Semiconducting Strontium Titanate. *Physical Review* **147,** 583–584 (1966).

48. Egerton, R. F. *The Scanning Electron Microscope* en. in *Physical Principles of Electron Microscopy* (Springer US, 2005), 125–153. ISBN: 978-0-387-25800-3, 978-0-387-26016-7.

49. Fabian, K., Shcherbakov, V. P. & McEnroe, S. A. Measuring the Curie temperature. en. *Geochemistry, Geophysics, Geosystems* **14,** 947–961 (2013).

50. Ziese, M. Critical scaling and percolation in manganite films. en. *Journal of Physics: Condensed Matter* **13,** 2919 (2001).

51. Savitzky, A. & Golay, M. J. E. Smoothing and Differentiation of Data by Simplified Least Squares Procedures. *Analytical Chemistry* **36,** 1627–1639 (1964).

52. Léon-Guevara, A. M. D., Berthet, P., Berthon, J., *et al.* Influence of controlled oxygen vacancies on the magnetotransport and magnetostructural phenomena in $La_{0.85}Sr_{0.15}MnO_{3-\delta}$ single crystals. *Physical Review B* **56,** 6031–6035 (1997).

53. Olsen, F. K. *Karakterisering av magnetiske egenskaper til (111)-orienterte funksjonelle grensesjikt basert på komplekse oksider* en. Master's Thesis (NTNU, Trondheim, 2015).

54. Berndt, L. M., Balbarin, V. & Suzuki, Y. Magnetic anisotropy and strain states of (001) and (110) colossal magnetoresistance thin films. *Applied Physics Letters* **77,** 2903–2905 (2000).

# Appendices

# Appendix A

# SCIL on the SUSS MA6

*This appendix gives detailed instructions for performing SCIL on the SUSS MA6 mask aligner at NTNU NanoLab. It is meant to be used as a user guide and troubleshooting guide for people with training on the MA6 at NanoLab.*

## A.1 SCIL Wafer Chuck Alignment

In order for conformal contact between stamp and sample to be possible, the surface of the substrate needs to be aligned with the surface of the SCIL wafer chuck. Alignment is performed by placing the sample in the wafer chuck, and using the micrometer screws on the chuck to raise the area surrounding the sample to the height of the sample surface. If irregular samples or samples with diameter other than 2 or 4 inches are used, an adapter is needed. The main text of this thesis gives suggestions for several different adapter designs that may be used. The most successful adapter design was found to be a flat surface covering the entire wafer chuck, with a through hole for the sample.

In order to ensure good height alignment, a microscope should be used. By focusing the microscope on the sample surface, and then adjusting the height wafer chuck until it also is in focus, one can iteratively get closer to perfect alignment by adjusting the height at the three corner locations. This process is repeated at 10x, 20x and 50x magnification.

If the yellow light microscope outside the lithography area is used, the insert of the microscope stage can be removed in order to get a more stable base for the wafer chuck.

## A.2 General Considerations

In order to perform SCIL with Amonil resist, the i-line filter needs to be removed from the mask aligner. According to the datasheet [42], Amonil requires an exposure dose of 5000 mJ/cm$^2$ at 320 nm in order to harden. Testing indicates that this exposure dose is indeed needed, as Amonil is soluble in acetone when unexposed, but insoluble when

hardened. After an exposure dose of 2000 mJ/cm$^2$, the resist was still easily soluble. Only NanoLab engineers and some power users are trained to remove the filter.

## A.3 MA6 Conversion to SCIL Mode

In order to use the MA6 mask aligner for SCIL, the instrument needs to be changed to SCIL mode.

1. Turn on the SCIL vacuum pump in the service finger.
2. Turn off the MA6 electronics (green switch).
3. Turn on the SCIL subassembly (switch on back). Wait for the subassembly to start up, and check that the readings on the front panel are OK. Figure A.1 shows the front panel of the SCIL subassembly.

**Figure A.1:** SUSS SCIL subassembly. Dial near top controls imprint pressure. Gauge in the middle shows imprint pressure. Displays near bottom show pressure (left) and vacuum (right).

4. Turn on the MA6 electronics (green switch). Wait for the system to boot up, and ensure that the SCIL subassembly (software version 0110) is loaded.
5. Remove the photolithography load frame by loosening the 4 thumbscrews, and lifting it up and out. Keep the load frame close to a surface at all times, in case the rubber o-rings have come out and are stuck to the load frame. If o-rings are stuck to the load frame, put them back onto the instrument. Figure A.2 shows a close-up of the instrument where o-rings are missing.

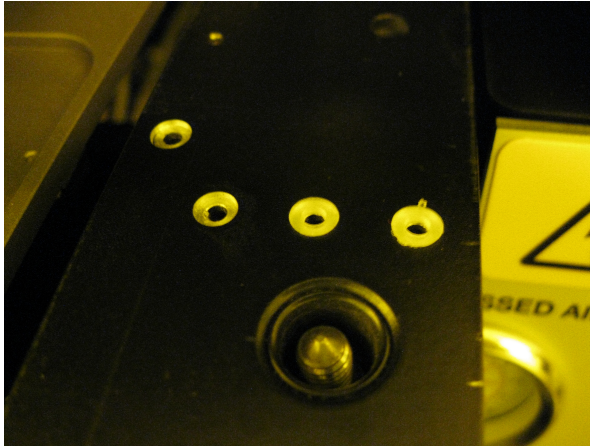

**Figure A.2:** Close-up of o-rings after removal of load frame. The two leftmost o-rings are missing.

6. Mount the SCIL load frame and tighten the 4 thumbscrews. Make sure not to damage the WEC spacers or electronics connector when inserting the load frame. Figure A.3 shows the SCIL load frame mounted on the mask aligner.

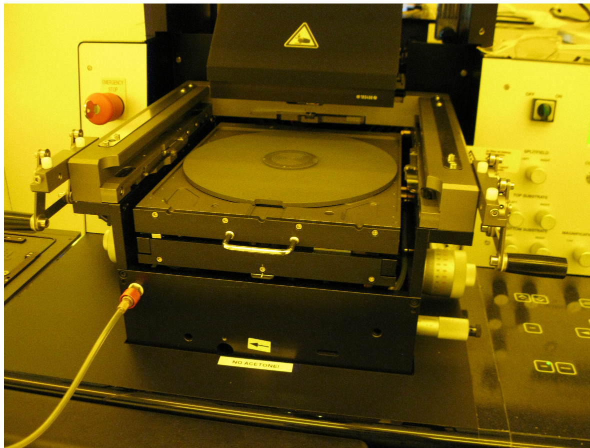

**Figure A.3:** SCIL load frame mounted on mask aligner.

7. Mount the SCIL connector block on the load frame and tighten the 2 thumbscrews. Ensure that the button on the right hand side of the block is in the depressed state.

## A.4 Performing SCIL

1. Change to the SCIL mask holder, and put the SCIL stamp on the mask holder. Enable the mask vacuum. Figure A.4 shows the SCIL mask holder with a SCIL stamp.

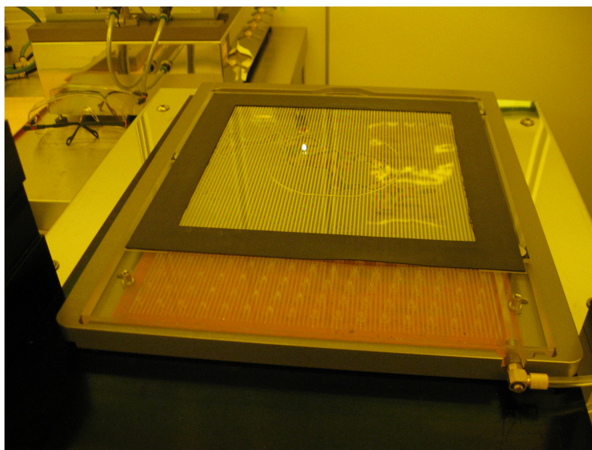

**Figure A.4:** SCIL stamp fixed to SCIL mask holder.

2. Load the mask holder into the instrument, and bring the connector block down. Press the button on the side of the connector block to connect the stamp to the SCIL vacuum. Ensure that the vacuum pressure reading on the SCIL subassembly increases to $\geq 50$. Some fiddling may be necessary before the SCIL subassembly recognizes that it has a vacuum seal and starts pumping. Figure A.5 shows the SCIL connector block in the loading and active (connected) positions.

3. Measure the 320 nm intensity using the SUSS UV optometer. After removing the wafer chuck from the instrument, the UV optometer can be inserted underneath the SCIL stamp. Figure A.6 shows the UV optometer in place of the wafer chuck.

4. Load the SCIL wafer chuck. The wafer chuck should be adjusted as described in Section A.1 before loading. Figure A.7 shows a wafer chuck with an adapter for $7.5 \times 7.5\,\text{mm}^2$ samples. The adapter is made from a 1.5 mm thick circuit board.

5. Adjust the SCIL imprint pressure using the dial on the SCIL subassembly. The reading is in kPa.

6. Program the software with desired parameters by pressing *Edit program*. If an exposure time exceeding 1000 s is required, press *Multiple exposure*. Table A.1

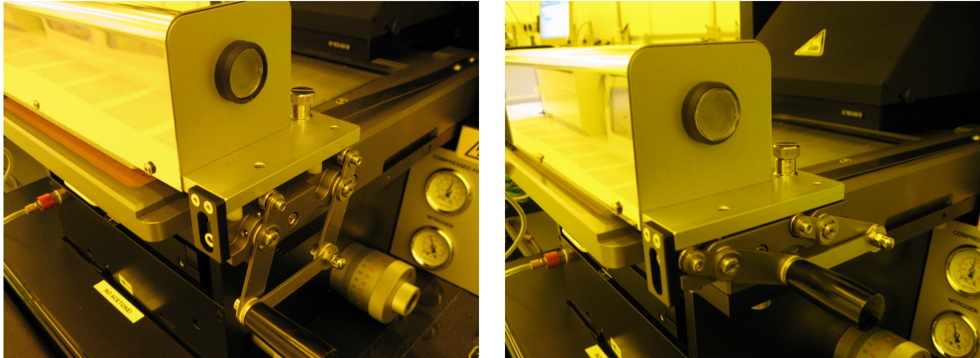

**(a)** Connector block up (button in) **(b)** Connector block down (button out)

**Figure A.5:** SCIL connector block in loading (up) and active (down) positions. The button on the side toggles the vacuum lines in the connector block. In the depressed state, the vacuum lines are disabled. In the unpressed state, the vacuum lines are active.

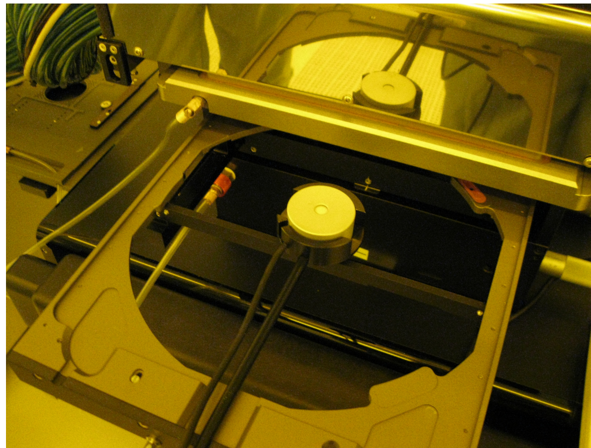

**Figure A.6:** UV optometer in place of the wafer chuck, before being pushed into the instrument for lamp test.

lists the software parameters, with a short explanation and sensible starting values.

7. Press *Load* and follow the on-screen instructions to perform WEC and sample alignment.

8. Press *Exposure* to start the process. Figure A.8 shows the mask aligner during exposure.

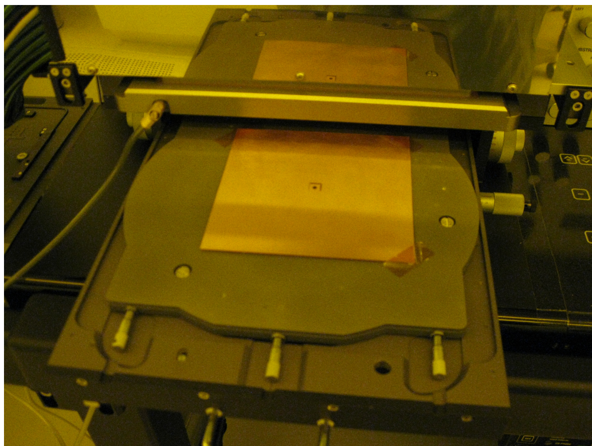

**Figure A.7:** SCIL wafer chuck with adapter loaded into MA6.

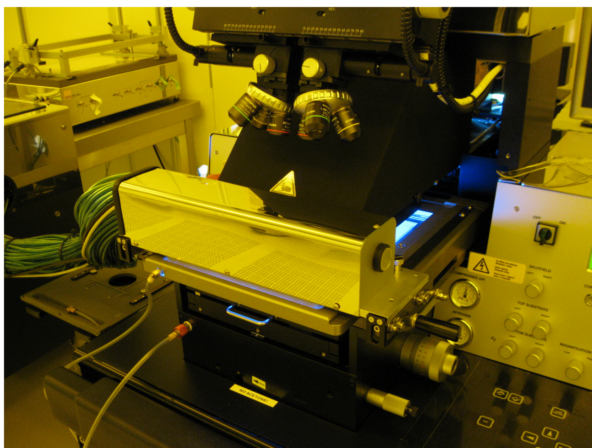

**Figure A.8:** SUSS MA6 mask aligner with SCIL subunit during exposure.

### A.4.1 Notes on SCIL Process Parameters

An imprint and separation step time of 3.0 s has been successfully used by the author, and is therefore listed in Table A.1. However, by watching the SCIL stamp holder during imprint, it is possible to see the stamp coming into contact with the resist as it moves across the sample. As described by Verschuuren [35], the movement is near-instantaneous, with the exeption of some pinning sites due to contamination on the stamp, stamp holder or wafer chuck. The step time needs to be long enough for these to be overcome. Based on these observations, a step time of 1.0 s should be sufficient.

**Table A.1:** List of process parameters in MA6 software with description.

| **Parameter** | **Description** | **Sensible Value** |
|---|---|---|
| Alignment gap | Gap between stamp and sample for alignment | 50 µm |
| WEC type | Whether to perform WEC in contact mode or use spacers on load frame | Cont |
| WEC offset | Offset for WEC using spacers | OFF |
| Process gap | Gap between stamp and sample when imprinting | 50 µm |
| Imprint area | Area of vacuum lines to use for imprinting. Must be multiple of 5. | *Size of stamp* |
| Exposure | Whether to UV expose the sample between imprint and separation | ON |
| Wait time | Delay between exposures if multiple exposure is enabled | 10 s |
| Cycles | Number of cycles for multiple exposure | |
| Exposure time | Exposure time for each cycle | *Calc. from UV intensity and required dose* |
| Step time imprint | Step time between flushing each vacuum line during imprinting | 3.0 s |
| Imprint direction | From which side to start flushing vacuum lines | *Be consistent* |
| Process delay | Delay after imprinting, before exposure | 240 s |
| Post process delay | Delay after exposure, before separation | 180 s |
| Step time separation | Step time between evacuating each vacuum line during separation | 3.0 s |
| Release direction | From which side to start evacuating vacuum lines | *Be consistent* |

### A.4.2 Aborting an Imprint

The SCIL subassembly communicates with the MA6 through a serial port. When the MA6 has commanded the SCIL subassembly to start imprinting, it cannot be stopped until it is done. If a problem occurs, and the imprint needs to be aborted, pressing *Unload* will **not** stop the imprint. Instead, it will complete imprinting, wait for the duration of the process delay, *skip exposure*, wait for the post process delay and then start separation. This will cause the features of the SCIL stamp to be filled with wet resist. In most cases, it is therefore wise to let the imprinting continue and expose the resist, even if a small problem has been spotted.

## A.5 MA6 Conversion to Lithography Mode

In order to convert the MA6 back to lithography mode, the steps taken to mount the SCIL equipment can be followed in the reverse order. It is important that the mask aligner is rebooted with the lithography load frame mounted, and the SCIL subassembly turned off, in order to be ready for the next photolithography user. Remember to turn off the SCIL vacuum pump in the service finger, even if the mask aligner is not to be turned off.

## A.6 Troubleshooting

**WEC fails with error "Loss of wafer vacuum"** This error may be triggered in several ways:

- Vacuum was lost when the wafer chuck was transferred from the frame to the WEC head. Fix: Adjust the chuck and try again.
- Mask aligner was booted with the wrong load frame.

  Fix: Turn off the electronics, switch to the photolithography frame, and turn electronics back on.
- Software was changed from Lithography mode to SCIL mode while in a mode that doesn't use WEC (e.g. flood exposure). Symptom: Display reads `SCIL /` in top left corner, rather than `SCIL / Cont`.

  Fix: Change software back to Lithography mode, and choose one of the contact modes (Soft/Hard/Vac). Then, change back to SCIL mode.

**Wafer stuck in stamp after imprinting** If the vacuum of the wafer chuck was not sufficient to allow the SCIL stamp to separate from the sample after imprinting, the sample may be stuck in the stamp.

Quick fix: Remove the stamp holder from the instrument, and place on SCIL subassembly. Wedge a 2A-SA (flat, round tip) tweezer between the sample and the stamp, while trying not to touch the stamp with the tweezer, as this will damage the stamp. Ethanol can be used as a lubricant, but may not be necessary.

Permanent fix: Use blue tape to ensure a good vacuum seal between sample and chuck.

**Instrument beeps with error "Axis out of range"** The X, Y, or rotation axis is outside the allowed range for SCIL. The movement of the wafer chuck is more restricted when using the SCIL load frame compared to the lithography load frame.

Fix: Adjust the micrometers in order to center the X and Y axes at the 10 mm marking, and align the cross to zero rotation.

# Appendix B

# Raw VSM Data

*This appendix contains figures showing the raw VSM data, as acquired before removing the diamagnetic contribution of the substrate and scaling to magnetic moment per manganese atom.*

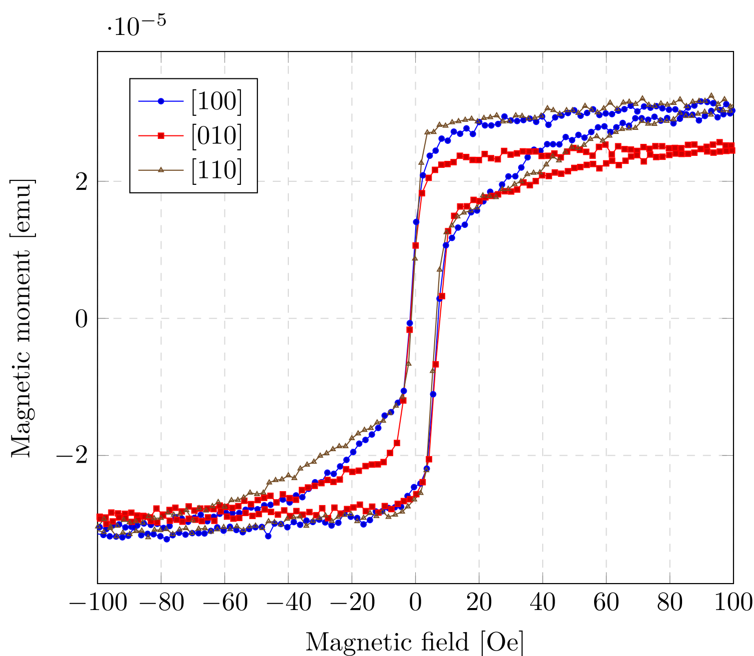


**Figure B.1:** Hysteresis curve for the unpatterned control sample along several crystal axes at 300 K, with a maximum applied field of ± 500 Oe.

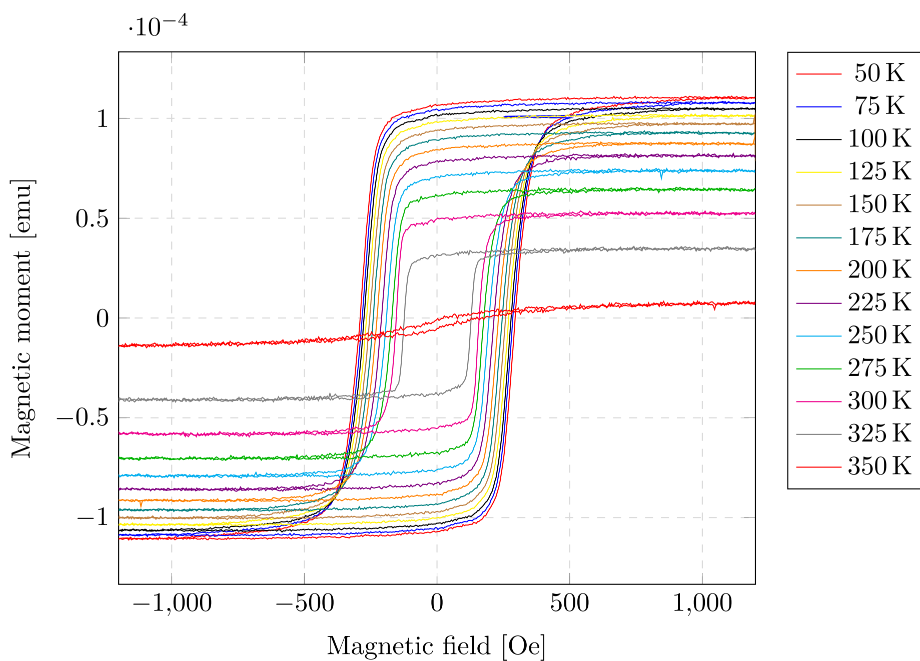


**Figure B.2:** Hysteresis curves of sample P50319 with field applied parallel with the nanoscale line pattern

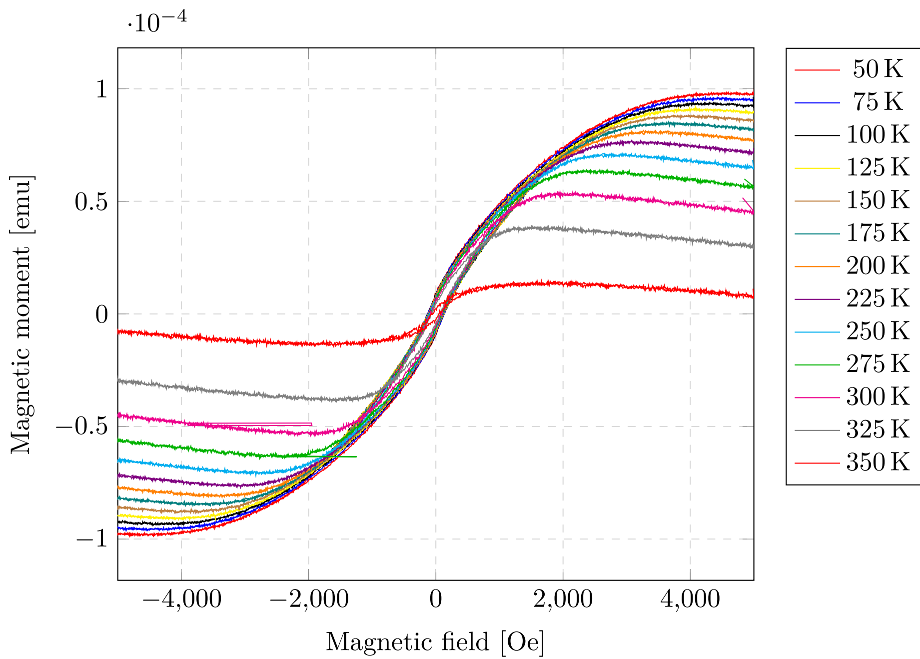


**Figure B.3:** Hysteresis curve of sample P50319 with field applied perpendicular to the nanoscale line pattern

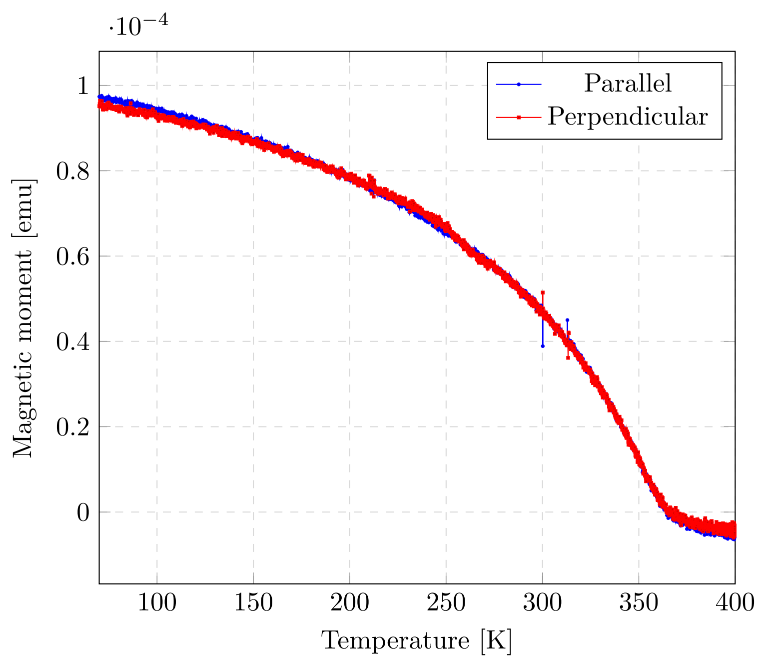


**Figure B.4:** Saturation magnetic moment as a function of temperature

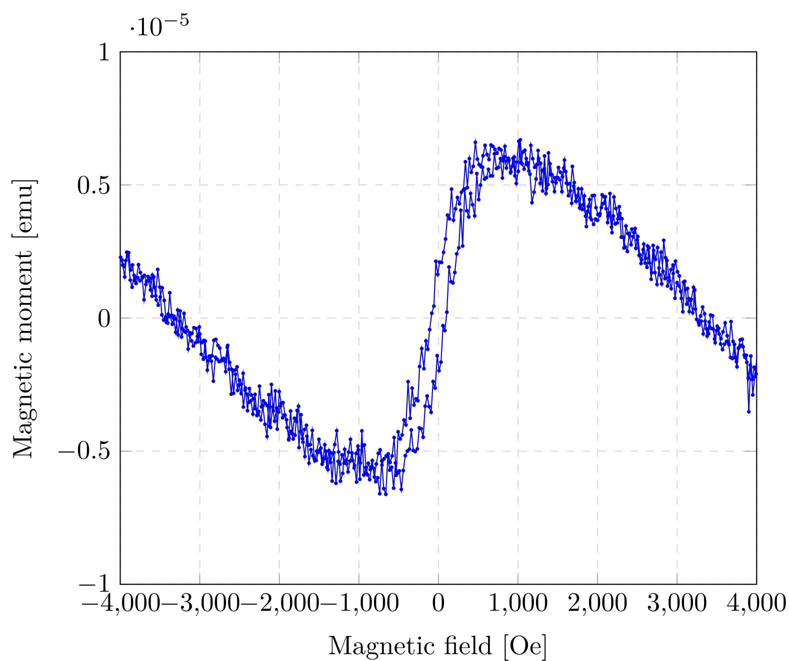


**Figure B.5:** Hysteresis curve of sample P50319 at 400 K with field applied parallel with the nanoscale line pattern